ARTICLE IN PRESS

Communications Materials

https://doi.org/10.1038/s43246-026-01190-1

Article in Press

Oxygen stoichiometry-driven charge compensation and Ruddlesden–Popper defects in ferromagnetic high-entropy manganite thin films

Received: 22 December 2025

Accepted: 4 May 2026

Cite this article as: Zhao, Z., Waqar, M., Jaiswal, A.K. *et al.* Oxygen stoichiometry-driven charge compensation and Ruddlesden–Popper defects in ferromagnetic high-entropy manganite thin films. *Commun Mater* (2026). https://doi.org/10.1038/s43246-026-01190-1

Zhibo Zhao, Moaz Waqar, Arun Kumar Jaiswal, Dirk Fuchs, Horst Hahn, Xiaoqing Pan, Robert Kruk & Abhishek Sarkar

We are providing an unedited version of this manuscript to give early access to its findings. Before final publication, the manuscript will undergo further editing. Please note there may be errors present which affect the content, and all legal disclaimers apply.

If this paper is publishing under a Transparent Peer Review model then Peer Review reports will publish with the final article.

ARTICLE IN PRESS

© The Author(s) 2026. **Open Access** This article is licensed under a Creative Commons Attribution 4.0 International License, which permits use, sharing, adaptation, distribution and reproduction in any medium or format, as long as you give appropriate credit to the original author(s) and the source, provide a link to the Creative Commons licence, and indicate if changes were made. The images or other third party material in this article are included in the article's Creative Commons licence, unless indicated otherwise in a credit line to the material. If material is not included in the article's Creative Commons licence and your intended use is not permitted by statutory regulation or exceeds the permitted use, you will need to obtain permission directly from the copyright holder. To view a copy of this licence, visit http://creativecommons.org/licenses/by/4.0/.

ARTICLE IN PRESS

Oxygen Stoichiometry–Driven Charge Compensation and Ruddlesden–Popper Defects in Ferromagnetic High-Entropy Manganite Thin Films

Zhibo Zhao[1,2], Moaz Waqar[3], Arun Kumar Jaiswal[4,#], Dirk Fuchs[4], Horst Hahn[1,2,5], Xiaoqing Pan[3,6,7], Robert Kruk[1,*], Abhishek Sarkar[8,*]

[1]Institute of Nanotechnology, Kaiserstraße. 12, Karlsruhe Institute of Technology, 76131 Karlsruhe, Germany

[2]KIT-TUD-Joint Research Laboratory Nanomaterials, Technical University Darmstadt, 64287 Darmstadt, Germany

[3]Department of Materials Science and Engineering, University of California, Irvine, CA, 92697 USA

[4]Institute for Quantum Materials and Technologies, Karlsruhe Institute of Technology, Kaiserstraße. 12, 76131 Karlsruhe, Germany

[5]Department of Materials Science & Engineering, The University of Arizona, Tucson, AZ, 210012 USA

[6]Department of Physics and Astronomy, University of California, Irvine, CA, 92697 USA

[7]Irvine Materials Research Institute, University of California, Irvine, CA, 92697 USA

[8]Department of Materials Science and Engineering, Indian Institute of Technology Delhi, Hauz Khas, New Delhi 110016, India

Corresponding authors: *robert.kruk@kit.edu*, *asarkar@iitd.ac.in*

Present address: Department of Quantum Matter Physics, University of Geneva, CH1211, Geneva 4, Switzerland

ARTICLE IN PRESS

ARTICLE IN PRESS

Abstract

High-entropy oxides (HEOs) originate from an innovative materials design strategy that stabilizes single-phase solid solutions despite the inclusion of multiple principal elements into a single cation sublattice. While prior efforts have largely focused on cation disorder, the impact of anion defects on the structure and properties of HEOs remains unexplored. Here, we examine the influence of oxygen non-stoichiometry on the nanostructure and magnetic properties of single-crystal high-entropy manganite (HE-Mn) films, $(Gd_{0.2}La_{0.2}Nd_{0.2}Sm_{0.2}Sr_{0.2})MnO_3$. The films were deposited on single-crystal $(LaAlO_3)_{0.3}(Sr_2AlTaO_6)_{0.7}$ (001) substrates under varying oxygen partial pressures $p(O_2)$. Phase-pure cube-on-cube epitaxy is maintained across all growth conditions. However, distinct nano-columnar Ruddlesden-Popper (RP) faults formed in oxygen deficient HE-Mn films. Unlike in conventional manganites, low-pressure-deposited films show no change in cation oxidation state, indicating the concurrent oxygen and manganese deficiency. This coupled cation-anion deficiency preserves the Mn^{3+}/Mn^{4+} ratio and drives RP fault formation. Consequently, ferromagnetic ordering persists even in the low $p(O_2)$ HE-Mn films, demonstrating their resilience to oxygen non-stoichiometry. Additionally, an *in-plane* to *out-of-plane* magnetic anisotropy crossover was observed, likely arising from spatial variation in the *c*-axis lattice constant. These findings establish oxygen non-stoichiometry as an effective control parameter for defect nanostructuring and magnetic property tuning in HEO epitaxial films.

ARTICLE IN PRESS

ARTICLE IN PRESS

1. Introduction

High-entropy oxides (HEOs) are a promising class of functional materials that offer access to a vast compositional space, enabling fine-tuning of properties.[1–6] The uniqueness of HEOs lies in their ability to retain phase-purity despite the presence of multiple principal cations on a given lattice site.[1,7–11] Consequently, the vastness of accessible composition space in HEOs provides the platform for extensive functionality design. Already HEOs are known for their enhanced electrochemical energy storage capabilities, high catalytic activities, superior ionic transport, tunable band gap and unique magnetic phenomena.[2,4,11–21] Most of the initial works on HEOs were carried out with powder or bulk ceramics.[22–24] Recent works have focused on fabrication of epitaxial HEO thin films, where substrate induced straining opens additional avenue for tuning their structure and properties.[25–28] Investigation on HEO thin films, although limited, showcase thickness and strain-dependent tuning of functional characteristics, such as magnetic transition temperatures, exchange bias, perpendicular magnetic anisotropy, etc.[26–29]

Oxygen deficiency, which results in oxygen vacancies (V_O) often accompanied by cation vacancies, profoundly impacts the structure and properties of oxide systems. Perovskite manganites are one such class of functional oxides, where the crystallographic structure, charge ordering, magnetic and electronic ground states are strongly affected by oxygen stoichiometry.[30,31] For instance, V_O can induce phase transition from perovskite to brownmillerite.[32] It is worth emphasizing that the structural modifications induced by V_O are intricately connected to changes in electronic and magnetic properties. For instance, precise control of oxygen content can significantly influence transport properties by modifying charge carrier density and triggering phenomena like the metal-insulator transition and colossal magnetoresistance.[30] Furthermore, V_O strongly affect the magnetism of manganite perovskites by modifying magnetic interactions, thereby influencing the Curie temperature (T_C) and saturation magnetization (M_S).[31,33]

In an earlier study, we explored HE-design strategy in combination with hole doping in manganite systems, $(Gd_{0.25}La_{0.25}Nd_{0.25}Sm_{0.25})_{1-x}Sr_xMnO_3$.[16] Investigations revealed single homogenous crystallographic structure with magnetic inhomogeneities in HE-manganites (HE-Mn), which manifests itself through an enhancement of colossal magnetoresistance (CMR) along with dual magnetic transitions.[16] Similar enhanced CMR has also been reported in other HE-Mn compositions, such as $(La_{0.2}Nd_{0.2}Pr_{0.2}Sm_{0.2}Eu_{0.2})_{1-x}Sr_xMnO_3$, where a structural transition from orthorhombic to rhombohedral symmetry with increasing Sr content was additionally observed[34]. It should be noted magnetic properties of HE-Mn (including CMR) are typically compared with conventional perovskite manganites (e.g., $La_{1-x}Sr_xMnO_3$)[16,34], rather than across different HEO classes, as magnetism in HEOs is highly structure dependent[7,8,23,24]. Even within perovskite-HEOs, A-site and B-site disorder can lead to contrasting magnetic behavior, with the B-site transition metal playing a dominant role [7,23,24,29]. Recently, we reported the influence of epitaxial strain on structure and magnetism of HE-Mn, where strained thin films $(Gd_{0.25}La_{0.25}Nd_{0.25}Sm_{0.25})_{0.8}Sr_{0.2}MnO_3$ exhibited a single ferromagnetic (FM) transition, unlike its bulk counterparts, along with a unique strain accommodation mechanism and substantial change

ARTICLE IN PRESS

in T_C.[27] In this study, we utilize different oxygen partial pressures, $p(O_2)$, during thin-film deposition, as the stimuli to tune the structure and magnetic properties of single crystal thin films of $(Gd_{0.2}La_{0.2}Nd_{0.2}Sm_{0.2}Sr_{0.2})MnO_3$, henceforth regarded as HE-Mn. Distinctive Ruddlesden-Popper (*RP*) faults are generated in oxygen-deficient HE-Mn thin films. Additionally, both T_C and M_S are suppressed in the films deposited at low oxygen pressures. However, HE-Mn show a higher tolerance to oxygen deficiency while preserving FM order, compared to conventional perovskite manganites. Overall, this work explored the effect of $p(O_2)$ during deposition and strain accommodation via defect formation in HE-Mn, and their subsequent impact on magnetic properties.

2. Results

2.1. Macroscopic and Nanoscale Structural Features

Figure 1 presents the macroscopic structural and surface topology characterization of the HE-Mn thin films at under three different $p(O_2)$. Our earlier work on epitaxial strain-dependent control of magnetic properties of the same HE-Mn compositions showed that $p(O_2)$ = 0.3 mbar results in optimal oxygen stoichiometry and magnetic properties identical to bulk HE-Mn.[27] Figure 1(a) shows a distinct shift of the diffraction peak to lower angles with decreasing $p(O_2)$ from 0.3 to 0.03 mbar. In the oxygen-optimized films grown at $p(O_2)$ = 0.3 mbar, the diffraction peak of HE-Mn (pseudo-cubic lattice parameter a_{pc} = 3.87 Å) coincides with that of the $(LaAlO_3)_{0.3}(Sr_2AlTaO_6)_{0.7}$, LSAT (001) substrate, reflecting the minimal lattice mismatch between them. Here, we use the terms *in-plane* (IP) and *out-of-plane* (OOP) strain to indicate the deviation from the bulk value a_{pc} = 3.87 Å. Clear Laue fringes are indicative of high-quality epitaxial growth and uniform film smoothness (Figure 1b). The ω-rocking curves (Figure 1c) demonstrate narrow full-width at half maximum (FWHM) values of 0.037°, 0.055°, and 0.056° for films deposited at $p(O_2)$ = 0.3 mbar, 0.15 mbar, and 0.03 mbar, respectively, indicating well-aligned crystal lattice planes and high epitaxial quality. Film thicknesses determined by X-ray reflectivity (XRR) show a slight variation of 25 nm (0.3 mbar), 30 nm (0.015 mbar), and 35 nm (0.03 mbar), despite identical deposition conditions. Higher $p(O_2)$ shortens the mean free path of ablated species therefore produces thinner films. Atomic force microscopy (AFM) micrographs (Figure 1d–f) confirm that all films have smooth surfaces with root-mean-square roughness (R_a) values of 0.13 nm ($p(O_2)$ = 0.03 mbar), 0.16 nm ($p(O_2)$ = 0.15 mbar), and 0.13 nm for, 0.15 mbar ($p(O_2)$ = 0. 3 mbar). These findings suggest that varying $p(O_2)$ have minimal influence on surface morphology while significantly affecting structural parameters such as lattice elongation.

Figure 2a displays RSMs, performed at (103) reflections, of HE-Mn thin films deposited on LSAT(001) under varying $p(O_2)$. For films deposited at 0.3 mbar (with stochiometric oxygen content), the diffraction peak of the HE-Mn film overlaps with that of the substrate, consistent with the X-ray diffraction (XRD) data in Figure 1a. Similarly, for the film deposited at 0.15 mbar, the diffraction pattern closely resembles that of the 0.3 mbar. However, a distinct thin-film signal

ARTICLE IN PRESS

intensity emerges for HE-Mn with 0.03 mbar $p(O_2)$, as indicated by the black arrow in Figure 2a. The alignment of q_x values between the thin film and substrate peaks towards lower values indicate the elongation of the OOP lattice parameter. Although XRD detects a slight peak shift for the 0.15 mbar sample, it is not possible to resolve the thin-film peak in the reciprocal-space maps (RSM). This discrepancy arises because symmetric, OOP XRD is highly sensitive to OOP strain and crystal quality, detecting minor variations in q_z. In the case of RSM, the thicker LSAT substrate dominates the RSM intensity, potentially masking the relatively low intense (103) thin-film peak when the lattice mismatch is minimal. Figure 2b illustrates the evolution of perpendicular strain, derived from the XRD-determined *c*-axis lattice parameters, as the $p(O_2)$ is lowered. This strain analysis reveals that oxygen-deficient HE-Mn thin films exhibit greater perpendicular strain and a pronounced elongation of the *c*-axis lattice parameter, reflecting the significant structural response of the films to oxygen non-stoichiometry.

Scanning transmission electron microscopy (STEM) characterization (**Figure 3** and **4**) was performed on HE-Mn thin films deposited at $p(O_2)$ of 0.3 mbar and 0.03 mbar. The film thicknesses determined from STEM are in good agreement with the XRR results (Supplementary Figure S1). For the oxygen-optimized film (0.3 mbar), the STEM images in Figure 3 reveal a defect-free, coherent interface with an orthorhombic crystal structure, as confirmed by the fast Fourier transform (FFT) in the inset of Figure 3b. The IP lattice strain extends coherently from the interface and gradually relaxes approximately 15 nm away, accompanied by a gradual decrease in the OOP lattice parameter, as shown in Figure 3c. This behavior reflects the progressive reduction of compressive strain with increasing distance from the LSAT substrate. Additionally, energy dispersive X-ray spectroscopy (EDS) analysis in Figure 3d indicates a uniform elemental distribution throughout the film, highlighting its compositional homogeneity.

For the oxygen-deficient thin film (0.03 mbar), STEM characterization in **Figure 4** highlights distinct structural features. The film exhibits coherent growth with the presence of columnar defects, as highlighted in the yellow box (Figure 4b). These defects are identified as Ruddlesden-Popper (RP) faults. The FFT pattern of the HE-Mn film deposited at 0.3 mbar (inset of Figure 3b) exhibits sharp and well-defined diffraction spots, indicating high crystallinity and a well-ordered perovskite structure with minimal structural defects. In contrast, the FFT pattern of the film grown at 0.03 mbar (inset of Figure 4a) shows elongated diffraction spots, accompanied by stronger diffuse scattering and more pronounced streaking. These features are characteristic of columnar defects (RP faults), which disrupt the lattice periodicity along the *c*-axis, confirming the formation of nanoscale RP intergrowths in the low oxygen pressure film. The RP faults appear 8-10 unit cells away from the film-substrate interface and play a key role in strain relaxation. It is worth mentioning that such RP faults, the best of our knowledge (based on an extensive literature survey, with representative examples cited in Refs.[16,25,26,28,36,37]), have not been reported for any HEO-based systems, either in bulk or thin-film form. It should be noted that an extensive literature survey has been done, a few references are Despite the presence of RP defects, the overall crystal structure remains orthorhombic and exhibits a high degree of structural integrity, especially at the sample-substrate interface, maintaining coherent strain both IP and OOP. The thickness profile in

ARTICLE IN PRESS

Figure 4c reveals an intriguing variation in the OOP lattice parameter, which initially increases with distance from the interface before decreasing closer to the film surface. This phenomenon is attributed to the strain-relaxation effects induced by RP defects, which introduce extra AO oxide layers into the perovskite lattice (Figure 4d, Supplementary Figure S2), disrupting the periodic stacking and relieving internal strain. Notably, the EDS analysis in Figure 4e confirms a homogeneous elemental distribution throughout the oxygen-deficient film, demonstrating that high V_O concentration does not compromise elemental uniformity. These results demonstrate that RP defects play a key role in accommodating strain and stabilizing the structure of oxygen-deficient HE-Mn films, while preserving compositional integrity.

2.2. Magnetic Properties

The magnetic behavior of HE-Mn is significantly influenced by oxygen deficiency stemming from the different deposition $p(O_2)$. The magnetization as a function of temperature (*M-T*) and magnetic field (*M-H*) data (**Figure 5**), reveal a clear trend of decreasing T_C and M_S with lower $p(O_2)$ during deposition. At $p(O_2)$ = 0.3 mbar, the HE-Mn thin film exhibits a T_C of 95 K. Reducing $p(O_2)$ to 0.15 mbar lowers T_C to 79 K, while the oxygen-deficient film (0.03 mbar) exhibits T_C as low as 40 K. The magnetic measurements indicate the presence of a ferromagnetically ordered state in all the samples, as evidenced by M_S and pronounced magnetic hysteresis. Similar to the variation in T_C, M_S also decreases with deposition $p(O_2)$, from 1.74 μ_B/f.u. (76.8 emu/g) at 0.3 mbar, to 1.36 μ_B/f.u. (59.5 emu/g) at 0.15 mbar, and to 0.88 μ_B/f.u. (36 emu/g) at 0.03 mbar.

The magnetic anisotropy, evaluated through *M-H* measurements at 5 K for both IP and OOP directions, shows notable variations with oxygen deposition pressure. At 0.3 mbar, the IP magnetization saturates at a lower field (4.1 T) than the OOP direction (5.3 T). For films deposited at 0.15 mbar, saturation occurs at reduced fields of 2.9 T (IP) and 3.2 T (OOP), indicating reduced anisotropy. At 0.03 mbar, the saturation behavior reverses, with the OOP direction saturating earlier (4.2 T) than the IP direction (5.4 T). This reversal IP to OOP easy axis upon lowering $p(O_2)$ suggests that increased V_O enhance perpendicular magnetic anisotropy (PMA) by altering local strain and crystal field environments.

To understand the combined effects of high cationic disorder and oxygen deficiency on the magnetism of HE-Mn thin films, we compared their magnetic properties with those of the parent $La_{0.7}Sr_{0.3}MnO_3$ (LSMO) thin films, exhibiting identical lattice parameters as bulk HE-Mn (3.875 Å) and deposited under identical conditions. $La_{0.7}Sr_{0.3}MnO_3$ was chosen as the reference composition to minimize lattice mismatch with the LSAT substrate, thereby reducing epitaxial strain and enabling a more direct comparison of intrinsic effects. Supplementary Figures S3 and S4 present the comparison of M_S and T_C for both HE-Mn and LSMO thin films as the function of $p(O_2)$ during deposition. At higher $p(O_2)$ (0.3 mbar and 0.15 mbar), LSMO thin films exhibit relatively stable ferromagnetic properties. The T_C remains nearly constant at 351 K and 350 K for $p(O_2)$ of 0.3 mbar and 0.15 mbar, respectively, while M_S decreases slightly from 4.81 μ_B/f.u. for 0.3 mbar to 4.10 μ_B/f.u. for 0.15 mbar. This stability correlates with the unchanged global structure observed in the XRD data for LSMO films at these oxygen pressures, highlighting the robust FM

ARTICLE IN PRESS

of LSMO under moderate oxygen deficiencies. In contrast, at a lower $p(O_2)$ of 0.03 mbar, both T_C and M_S in LSMO undergo a drastic reduction, signaling a collapse of FM order due to severe oxygen deficiency. This sharp decline contrasts with the more gradual reduction of T_C and M_S observed in HE-Mn films across the same range of oxygen pressures. These differences underscore the enhanced tolerance of HE-Mn films to oxygen deficiency, likely due to their high ionic disorder and unique strain-charge-compensation mechanisms, as discussed earlier. The comparison reveals that oxygen deficiency has a much stronger detrimental effect on the FM ordering in LSMO than on HE-Mn, emphasizing the resilience of HEO (in general) under conditions of oxygen non-stoichiometry.

To provide a clearer comparison, **Figure 6** plots the relative variations in Curie temperature and saturation magnetization as a function of oxygen pressure for HE-Mn and LSMO thin films. The reference LSMO films show relatively stable T_C and M_S at 0.3 mbar and 0.15 mbar with minimal changes. However, when the oxygen pressure is reduced to 0.03 mbar, both T_C and M_S exhibit a drastic drop of over 85% compared to their values in oxygen-stoichiometric conditions (T_C relative to bulk, and M_S relative to the oxygen-stoichiometric LSMO film). In contrast, the HE-Mn thin films exhibit a nearly linear decrease in both T_C and M_S with decreasing oxygen pressure, reflecting a more gradual response to oxygen deficiency. From 0.3 mbar to 0.15 mbar, M_S in HE-Mn decreases by 22%, a much larger change than the corresponding 5.2% reduction in LSMO. However, as $p(O_2)$ is further reduced to 0.03 mbar, the decrease in M_S for HE-Mn is 53%, which remains significantly less severe than the 89% reduction observed for LSMO under the same conditions. As discussed later, it is important to note that the Mn oxidation state remains largely unchanged in the case of HE-Mn with variation in the $p(O_2)$. This might be one of the prime reasons for the contrasting trend observed in the variations of T_C, where HE-Mn films show a more gradual decline compared to the abrupt collapse in LSMO. These results further underscore the enhanced resilience of HE-Mn films to oxygen non-stoichiometry.

ARTICLE IN PRESS

3. Discussion

Similar to conventional LSMO, oxygen deficiency stemming from the lower deposition $p(O_2)$ in HE-Mn is expected to induce three primary effects: breaking of Mn-O-Mn bonds, creating local Mn-O_6 octahedra distortions, and reduction of Mn^{4+} to Mn^{3+} ions. Their synergistic impact is evident from the expansion of the OOP lattice parameter as observed in the XRD data (Figure 1a). In oxygen-deficit LSMO epitaxial thin films, several interrelated factors result in the elongation of the OOP lattice parameter. First, V_O disrupt and weakens the Mn-O bond network[33]. This disruption results in the relaxation of the crystal lattice and increases the *c*-axis length to accommodate altered bonding. Second, the oxygen deficiency usually drive the reduction of Mn^{4+} to Mn^{3+} as a charge compensation mechanism. Mn^{3+} (0.645 Å) is larger than Mn^{4+} (0.53 Å), which results in the lattice expansion, particularly along the *c*-axis (OOP), as the IP lattice parameter is fixed by the substrate[38]. Moreover, Mn^{3+} lead to pronounced Jahn-Teller effect, accompanied by elongation along specific directions. Finally, the elongation can also be attributed to increased

ARTICLE IN PRESS

Coulomb repulsion stemming from the V_O mediated local charge imbalances[39]. As a result, the lattice is stretched along *c*-axis as the neighboring cations are pushed apart.

Detailed STEM analysis of the HE-Mn thin films deposited at the highest and lowest $p(O_2)$ was performed to investigate the spatial evolution of the IP and OOP lattice parameters and the possible structural relaxation mechanisms. The oxygen stoichiometric HE-Mn deposited at 0.3 mbar exhibits an IP lattice parameter (blue in Figure 3c) that remains essentially constant throughout its entire thickness. Furthermore, similarity between the IP and OOP lattice parameter (a = 3.832 Å) indicates the optimal oxygen stoichiometry of the film. In contrast, when the HE-Mn films were deposited at 0.03 mbar, the IP lattice spacing remains fixed, while the OOP lattice parameter stays expanded up to the near-surface region. Despite the substantial oxygen deficiency, stemming from the low $p(O_2)$ deposition, the film does not lose epitaxy. This unexpected coherence arises from the development of vertically oriented, nanoscale Ruddlesden–Popper (RP) fault segments, as depicted in the STEM images (Figure 4b). RP faults, described by $A_{n+1}B_nO_{3n+1}$, consists of rocksalt-type AO sheets that are alternately stacked with perovskite blocks. The AO layers offer local strain-relief pathways, allowing the oxygen-deficient HE-Mn to retain the epitaxy with the LSAT substrate. The nanoscale-RP faults in HE-Mn, can be represented by the formula $(Gd_{0.2}La_{0.2}Nd_{0.2}Sm_{0.2}Sr_{0.2})_2MnO_4$, which includes a rocksalt layer represented by the formula $(Gd_{0.2}La_{0.2}Nd_{0.2}Sm_{0.2}Sr_{0.2})O$. RP-type defects are known to appear in conventional perovskites when certain growth conditions are met, such as high deposition rates that produce numerous nuclei with incomplete of the growing layers[40]. Deviations in the A-site/B-site ratio, whether due to growth kinetics or intentional target design, can also stabilize RP stacking. Excess of A-site cations (e.g., Sr-rich $SrTiO_3$ and Sm-rich $SmNiO_3$)[41,42] tends to promote displaced AO layers that form RP faults, relieving (epitaxy-induced) lattice strain and improving structural stability[43].

The presence of RP faults in HE-Mn therefore points to an excess of A-site rare-earth ions relative to Mn. A series of spectroscopic experiments (Supplementary Figure S5 and S6) were done for both RE and Mn ions to evaluate the validity of the aforementioned hypothesis. Interestingly, EELS measurements (**Figure 7**a) highlight that the Mn oxidation state remains essentially unchanged between the 0.3 and 0.03 mbar samples. This is distinct from conventional manganites, where Mn^{4+} readily converts to Mn^{3+} under lower $p(O_2)$ depositions, such as in LSMO. This dictates that oxygen-deficiency in HE-Mn do not reduce Mn oxidation state, but instead promote the formation of nanoscale RP structures. Complementary O-*K* edge spectra (Figure 7b) reveal modifications in local bonding environments, plausibly originating from the deficiency in oxygen. Figure 7c indicates that these O-*K* edge characteristics are not confined to the RP faults but are consistently observed across the entire oxygen deficit HE-Mn film. Given the substantial oxygen deficiency without Mn oxidation reduction, the mechanism for charge compensation becomes a key question. One possibility is reduction of Sm^{3+} to Sm^{2+}, since Sm is only other cation in the HE-Mn that can exhibit mixed valence, as other RE ions typically remain trivalent, while Sr is stable 2+. However, EELS measurements of Sm and other RE ions (Supplementary Figure S5) reveal no significant shifts indicative of a change in oxidation state. Small energy shifts observed

ARTICLE IN PRESS

for La, Nd, and Gd (Supplementary Figure S5) at lower $p(O_2)$ likely reflect changes in local electron density rather than actual changes in valence.

These defect and charge-compensation processes strongly influence magnetic behavior, distinguishing HE-Mn from conventional LSMO. In both systems, oxygen deficiency lowers the T_C and M_S, but the rate and magnitude of these changes differ. LSMO exhibits a steep decline due to the collapse of double-exchange pathways as Mn^{4+} converts to Mn^{3+}. In HE-Mn, however, Mn maintains its +4 state, preventing the enhancement of the antiferromagnetic interactions typically induced by V_O. Moreover, the local strain introduced by oxygen deficiency is partly accommodated by RP faults, which further suppress the destabilizing effects typically observed in oxygen-deficient conventional manganites. As a result, while LSMO supports FM only within a narrow oxygen-stoichiometric window, HE-Mn retains FM order across a much broader range of oxygen stoichiometry. These fundamental findings warrant further element-specific magnetic measurements, such as X-ray magnetic circular and linear dichroism, particularly at the Mn edges, complemented by theoretical investigations to provide deeper insight into the mechanisms of strain accommodation and the evolution of magnetic properties in HE–Mn films.

Another notable observation is the dependence of magnetic anisotropy on oxygen content. Films grown at $p(O_2)$ = 0.03 mbar exhibit signatures of emerging perpendicular magnetic anisotropy. This behavior can be linked to the columnar RP segments produced by V_O, which interrupt the periodic perovskite network by inserting rock-salt AO layers. This structural disruption plausibly breaks the IP symmetry, resulting in local anisotropic strain favoring OOP magneto-crystalline anisotropy. Hence, the magnetization easy axis shifts toward the perpendicular direction. Overall, adjusting the oxygen content provides an effective route for tuning magnetic responses in the HE-Mn systems, making oxygen stoichiometry a powerful tool for engineering their functional magnetic properties.

4. Conclusions

This work demonstrates how controlled oxygen pressure $p(O_2)$ during pulsed laser deposition influences the structure and magnetic properties of epitaxial HE-Mn thin films deposited on LSAT substrates. Single-crystal thin films with surface roughness below 0.17 nm are obtained independent of the deposition condition. A strong impact of $p(O_2)$ is observed, manifesting as significant *c*-axis elongation along with nano-columnar Ruddlesden-Popper (RP) defects in films deposited under the lowest $p(O_2)$. RP defects, which to the best of our knowledge are unreported in HEOs, facilitate strain relaxation and support defect-free epitaxial growth at the interface. Unlike conventional manganites such as $La_{0.7}Sr_{0.3}MnO_3$ (LSMO), Mn^{4+} reduction to Mn^{3+} is not observed. Instead, the stable Mn^{3+}/Mn^{4+} ratio observed in the perovskite matrix, irrespective of oxygen deposition pressure, is attributed to the presence of Mn-vacancies that accompany oxygen vacancies. The Mn-vacancies drives the formation of local RP defects. This unique charge compensation mechanism, coupled with RP-induced strain relaxation results in distinct magnetic behavior compared to LSMO. A robust ferromagnetic ordering along with enhanced out-of-plane magneto-crystalline anisotropy is observed in HE-Mn deposited at lower oxygen pressures. This

ARTICLE IN PRESS

work highlights the tolerance of oxygen non-stoichiometry in HE-Mn, establishing a basis for tailoring their functional properties through strain modulation and oxygen vacancy engineering.

5. Methods

Thin film growth: Epitaxial HE-Mn layers were synthesized on (001)-oriented single-crystal substrates of LSAT, utilizing pulsed laser deposition (PLD) technique. The HE-Mn ceramic target was synthesized in-house, details are provided in elsewhere.[27,35] A KrF excimer source (λ = 248 nm) was operated at 2 Hz for a total of 2000 pulses to ablate the ceramic target, with the laser fluence maintained at 1.68 J/cm^2. After the growth, the films were cooled to 25 ^{o}C at a rate of 20 ^{o}C min^{-1} while preserving the deposition atmosphere.[27,35] The oxygen stoichiometry was controlled using three different $p(O_2)$ for deposition: 0.3, 0.15, and 0.03 mbar. All other deposition parameters were kept constant. For comparison of the magnetic behaviour, $La_{0.7}Sr_{0.3}MnO_3$ (LSMO) reference films were fabricated under the same processing conditions, including identical laser settings and cooling protocol.

Characterization: XRR, XRD, rocking-curve (ω-scans), and RSM were carried out on a Bruker D8 Davinci system employing Cu Kα radiation. Surface morphology was assessed utilizing a Bruker Dimension Icon AFM operated in tapping mode, with images recorded over a 2-µm scan area (512 lines per frame) at a 1 Hz scan rate. High-resolution STEM and EDS were performed at the Irvine Materials Research Institute, University of California, Irvine, using an aberration-corrected JEM-300CF microscope operated at 300 keV and equipped with dual SDD detectors and a Gatan K2 Summit camera.

Magnetic properties were probed using a Quantum Design MPMS3 SQUID magnetometer. The *M-T* and *M-H* was measured over the temperature range of 5–380 K and within applied fields ranging from −7 T to +7 T. For accurate background subtraction, given that commercially obtained LSAT substrates do not always behave as perfect diamagnets, we treated the LSAT substrates under conditions identical to those used for the deposition of the HEO films (temperature, vacuum, and duration). The magnetization of these treated substrates was then measured (*M–T* and *M–H*) using SQUID. The final magnetic response of the HEO thin films was obtained by subtracting these contributions to isolate the film signal as accurately as possible.

Author Contributions

Z.Z. and A.S. conceived the project and designed the experiments. Z.Z. fabricated the samples and performed XRR, XRD and rocking curve, AFM and SQUID measurements. A.K.J. and D.F. performed the RSM measurements. X.P. and M.W. performed the STEM measurements and analysis. A.S., R.K., X.P. and H.H. supervised the project. Z.Z., A.S. and R.K. wrote the manuscript with comments from other authors.

ARTICLE IN PRESS

Data availability

All data supporting the findings of this study are either included in the article and supplementary information (SI) or are available from the corresponding author(s) upon reasonable request.

Competing interests

The authors declare no competing interests.

Acknowledgements

Z.Z., R.K. and H.H. acknowledge the support from the European Union's Horizon 2020 research and innovation program under the Marie Skłodowska-Curie grant agreement No. 861145. AS and HH acknowledge financial support from the Deutsche Forschungsgemeinschaft (DFG) project HA 1344/43-2. X.P. and M.W. acknowledge the financial support from the National Science Foundation Materials Research Science and Engineering Centre program through the UC Irvine Center for Complex and Active Materials (DMR-2011967). A.K.J. acknowledges financial support from the European Union's Framework Programme for Research and Innovation, Horizon 2020, under the Marie Skłodowska-Curie grant agreement No. 847471 (QUSTEC). We acknowledge support by the KIT-Publication Fund of the Karlsruhe Institute of Technology.

ARTICLE IN PRESS

Funding declaration

Deutsche Forschungsgemeinschaft (DFG) project HA 1344/43-2.
Marie Skłodowska-Curie grants No. 861145 and No. 847471.
National Science Foundation Materials Research Science and Engineering Centre project DMR-2011967.

References

1. Sarkar, A. *et al.* High-Entropy Oxides: Fundamental Aspects and Electrochemical Properties. *Advanced Materials* **31**, 1806236 (2019).

2. Aamlid, S. S., Oudah, M., Rottler, J. & Hallas, A. M. Understanding the Role of Entropy in High Entropy Oxides. *J. Am. Chem. Soc.* **145**, 5991–6006 (2023).

3. Ma, Y. *et al.* High-entropy energy materials: challenges and new opportunities. *Energy Environ. Sci.* **14**, 2883–2905 (2021).

4. Musicó, B. L. *et al.* The emergent field of high entropy oxides: Design, prospects, challenges, and opportunities for tailoring material properties. *APL Mater.* **8**, 040912 (2020).

5. Wang, Q., Velasco, L., Breitung, B. & Presser, V. High-Entropy Energy Materials in the Age of Big Data: A Critical Guide to Next-Generation Synthesis and Applications. *Adv. Energy Mater.* **11**, 2102355 (2021).

ARTICLE IN PRESS

6. Rost, C. M. *et al.* Entropy-stabilized oxides. *Nat. Commun.* **6**, 8485 (2015).

7. Sarkar, A., Breitung, B. & Hahn, H. High entropy oxides: The role of entropy, enthalpy and synergy. *Scr. Mater.* **187**, 43–48 (2020).

8. Sarkar, A., Kruk, R. & Hahn, H. Magnetic properties of high entropy oxides. *Dalton Transactions* **50**, 1973–1982 (2021).

9. Sarkar, A. *et al.* Rare earth and transition metal based entropy stabilised perovskite type oxides. *J. Eur. Ceram. Soc.* **38**, 2318–2327 (2018).

10. Fracchia, M., Coduri, M., Manzoli, M., Ghigna, P. & Tamburini, U. A. Is configurational entropy the main stabilizing term in rock-salt Mg0.2Co0.2Ni0.2Cu0.2Zn0.2O high entropy oxide? *Nat. Commun.* **13**, 2977 (2022).

11. Fracchia, M. *et al.* Stabilization by Configurational Entropy of the Cu(II) Active Site during CO Oxidation on Mg 0.2 Co 0.2 Ni 0.2 Cu 0.2 Zn 0.2 O. *J. Phys. Chem. Lett.* **11**, 3589–3593 (2020).

12. Oses, C., Toher, C. & Curtarolo, S. High-entropy ceramics. *Nat. Rev. Mater.* **5**, 295–309 (2020).

13. Sarkar, A. *et al.* High entropy oxides for reversible energy storage. *Nat. Commun.* **9**, 3400 (2018).

14. Su, L. *et al.* Direct observation of elemental fluctuation and oxygen octahedral distortion-dependent charge distribution in high entropy oxides. *Nat. Commun.* **13**, 2358 (2022).

15. Lin, C.-C. *et al.* In-situ X-ray studies of high-entropy layered oxide cathode for sodium-ion batteries. *Energy Storage Mater.* **51**, 159–171 (2022).

16. Sarkar, A. *et al.* High Entropy Approach to Engineer Strongly Correlated Functionalities in Manganites. *Advanced Materials* **35**, 2207436 (2023).

17. Sarkar, A. *et al.* Determining role of individual cations in high entropy oxides: Structure and reversible tuning of optical properties. *Scr. Mater.* **207**, 114273 (2022).

18. Sharma, N. *et al.* Large exchange bias effect and complex magnetism in a tetragonal high entropy spinel oxide. *Appl. Phys. Lett.* **123**, (2023).

19. Dąbrowa, J. *et al.* Structure and transport properties of the novel (Dy,Er,Gd,Ho,Y)3Fe5O12 and (Dy,Gd,Ho,Sm,Y)3Fe5O12 high entropy garnets. *J. Eur. Ceram. Soc.* **41**, 3844–3849 (2021).

20. Biesuz, M. *et al.* Ni-free high-entropy rock salt oxides with Li superionic conductivity. *J. Mater. Chem. A Mater.* **10**, 23603–23616 (2022).

21. Velasco, L. *et al.* Phase–Property Diagrams for Multicomponent Oxide Systems toward Materials Libraries. *Advanced Materials* **33**, 2102301 (2021).

22. Spiridigliozzi, L. *et al.* Ultra-fast high-temperature sintering (UHS) of Ce0.2Zr0.2Y0.2Gd0.2La0.2O2−δ fluorite-structured entropy-stabilized oxide (F-ESO). *Scr. Mater.* **214**, 114655 (2022).

23. Witte, R. *et al.* High-entropy oxides: An emerging prospect for magnetic rare-earth transition metal perovskites. *Phys. Rev. Mater.* **3**, 034406 (2019).

ARTICLE IN PRESS

24. Witte, R. *et al.* Magnetic properties of rare-earth and transition metal based perovskite type high entropy oxides. *J. Appl. Phys.* **127**, 185109 (2020).

25. Sharma, Y. *et al.* Magnetic anisotropy in single-crystal high-entropy perovskite oxide La(Cr0.2Mn0.2Fe0.2Co0.2Ni0.2)O3. *Phys. Rev. Mater.* **4**, 014404 (2020).

26. Zhao, Z. *et al.* Strain-Driven Bidirectional Spin Orientation Control in Epitaxial High Entropy Oxide Films. *Advanced Science* **10**, (2023).

27. Zhao, Z. *et al.* Strained single crystal high entropy oxide manganite thin films. *Appl. Phys. Lett.* **125**, (2024).

28. Sharma, Y. *et al.* Magnetic Texture in Insulating Single Crystal High Entropy Oxide Spinel Films. *ACS Appl. Mater. Interfaces* **13**, 17971–17977 (2021).

29. Mazza, A. R. *et al.* Designing Magnetism in High Entropy Oxides. *Advanced Science* **9**, 2200391 (2022).

30. Cao, L. *et al.* Reversible Control of Physical Properties via an Oxygen-Vacancy-Driven Topotactic Transition in Epitaxial $La_{0.7}Sr_{0.3}$ $MnO_{3-\delta}$ Thin Films. *Advanced Materials* **31**, (2019).

31. Zhao, R. *et al.* The oxygen vacancy effect on the magnetic property of the LaMnO3−δ thin films. *Appl. Phys. Lett.* **102**, (2013).

32. Ferguson, J. D. *et al.* Epitaxial Oxygen Getter for a Brownmillerite Phase Transformation in Manganite Films. *Advanced Materials* **23**, 1226–1230 (2011).

33. Kumari, S. *et al.* Effects of Oxygen Modification on the Structural and Magnetic Properties of Highly Epitaxial La0.7Sr0.3MnO3 (LSMO) thin films. *Sci. Rep.* **10**, 3659 (2020).

34. Kumar, A. *et al.* Magnetic and electrical properties of high-entropy rare-earth manganites. *Materials Today Physics* **32**, 101026 (2023).

35. Zhao, Z. Tuning of Magnetism in High Entropy Oxide Thin Films. (Technische Universität Darmstadt, 2025).

36. Kotsonis, G. N. *et al.* Property and cation valence engineering in entropy-stabilized oxide thin films. *Phys. Rev. Mater.* **4**, 100401 (2020).

37. Johnstone, G. H. J. *et al.* Entropy Engineering and Tunable Magnetic Order in the Spinel High-Entropy Oxide. *J. Am. Chem. Soc.* **144**, 20590–20600 (2022).

38. Song, C. *et al.* Hidden metal-insulator transition in manganites synthesized via a controllable oxidation. *Sci. China Mater.* **62**, 577–585 (2019).

39. Sakai, J., Ito, N. & Imai, S. Oxygen content of La1−xSrxMnO3−y thin films and its relation to electric-magnetic properties. *J. Appl. Phys.* **99**, 08Q318 (2006).

40. Xu, C. *et al.* Formation mechanism of Ruddlesden-Popper-type antiphase boundaries during the kinetically limited growth of Sr rich SrTiO3 thin films. *Sci. Rep.* **6**, 38296 (2016).

41. Zhong, Q. *et al.* Revealing a high-density three-dimensional Ruddlesden–Popper-type fault network in an SmNiO3 thin film. *J. Mater. Res.* **36**, 1637–1645 (2021).

ARTICLE IN PRESS

ARTICLE IN PRESS

42. Tokuda, Y. *et al.* Growth of Ruddlesden-Popper type faults in Sr-excess SrTiO3 homoepitaxial thin films by pulsed laser deposition. *Appl. Phys. Lett.* **99**, (2011).

43. Qi, H. *et al.* Formation mechanism of Ruddlesden–Popper faults in compressive-strained ABO_3 perovskite superlattices. *Nanoscale* **13**, 20663–20669 (2021).

ARTICLE IN PRESS

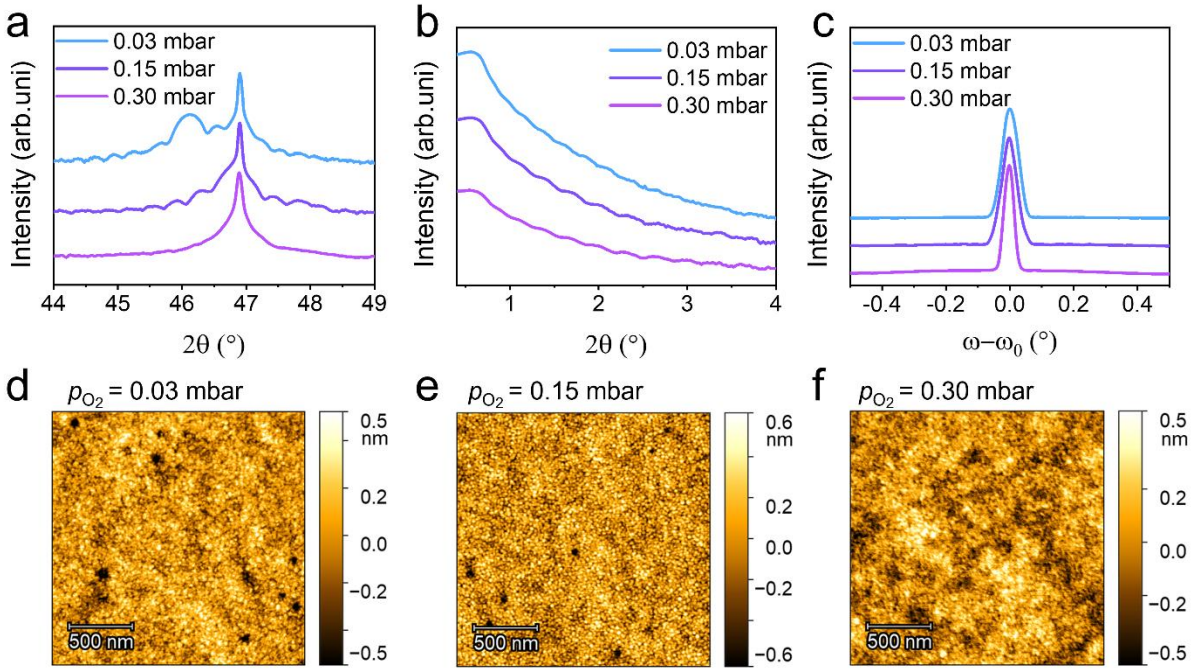

Figure 1. a HR-XRD, **b** XRR, and **c** ω-rocking curves, showcasing epitaxial growth of HE-Mn films deposited at different $p(O_2)$ on LSAT (001). **d** AFM of HE-Mn thin films indicating smooth surface topology.

ARTICLE IN

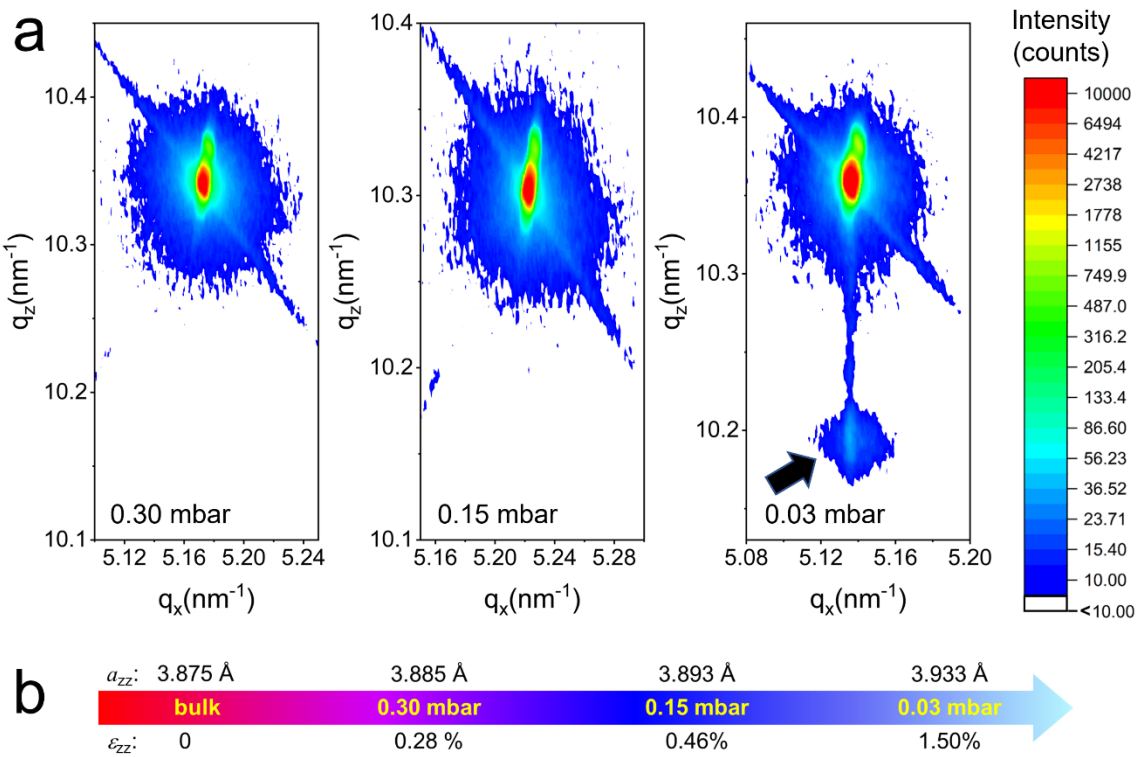

Figure 2. RSM in the vicinity of the (103) reflection of LSAT and c-axis lattice mismatch in HE-Mn thin films. **a** RSM of HE-Mn thin films. **b** corresponding perpendicular tensile strain (ε_{zz}, bottom) and distorted *c*-axis lattice parameter (a_{zz}, top). Black arrow denotes HE-Mn diffraction signal.

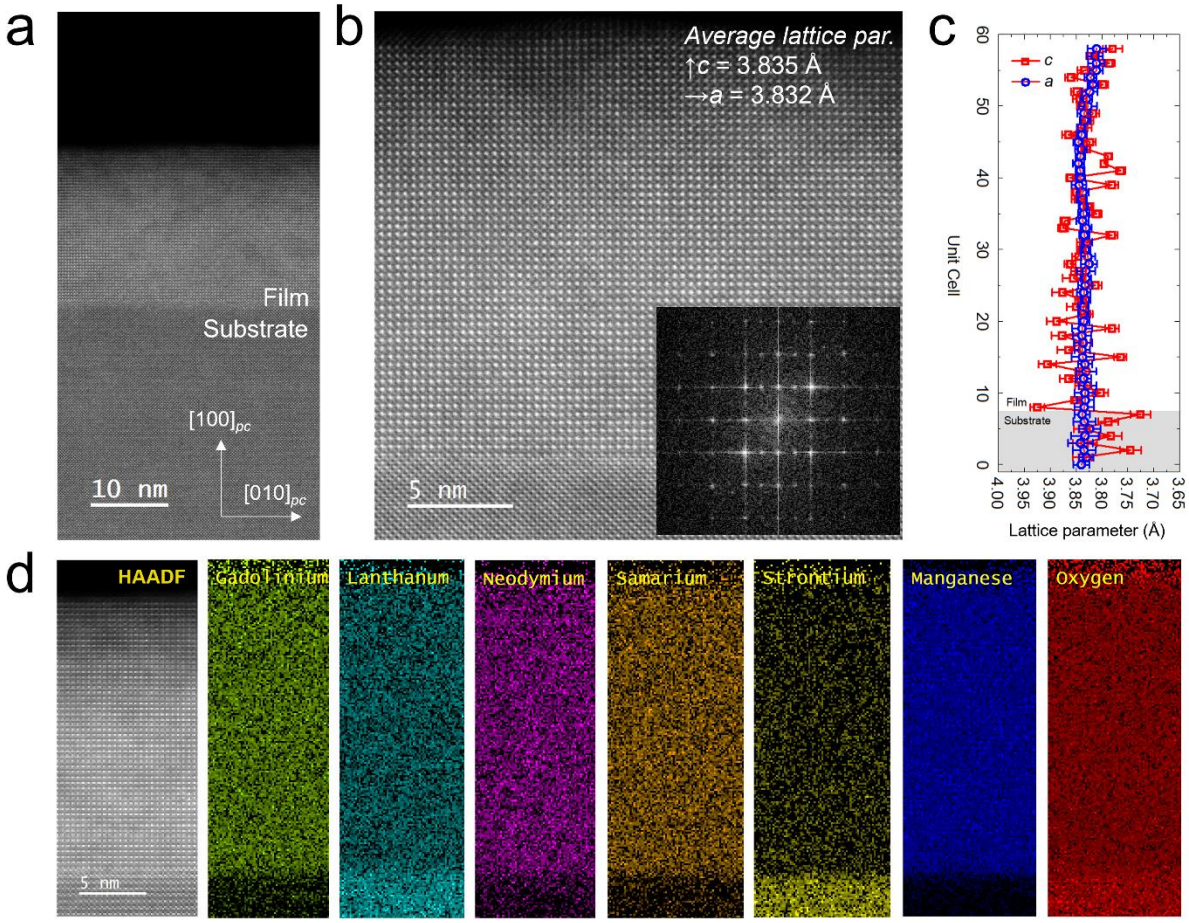

Figure 3. STEM analysis of HE-Mn deposited under $p(O_2)$ = 0.3 mbar. **a**, **b** High resolution HAADF-STEM micrographs along [001] direction, indicating coherent and defect free growth of HE-Mn on LSAT, inset Fast Fourier transform (FFT) analysis reveals well-defined diffraction spots, confirming the high crystallinity and epitaxial growth of the film on the LSAT substrate. **c** Profile of lattice parameter and unit cell from interface. **d** EDS mapping depicting uniform elemental distribution in HE-Mn films.

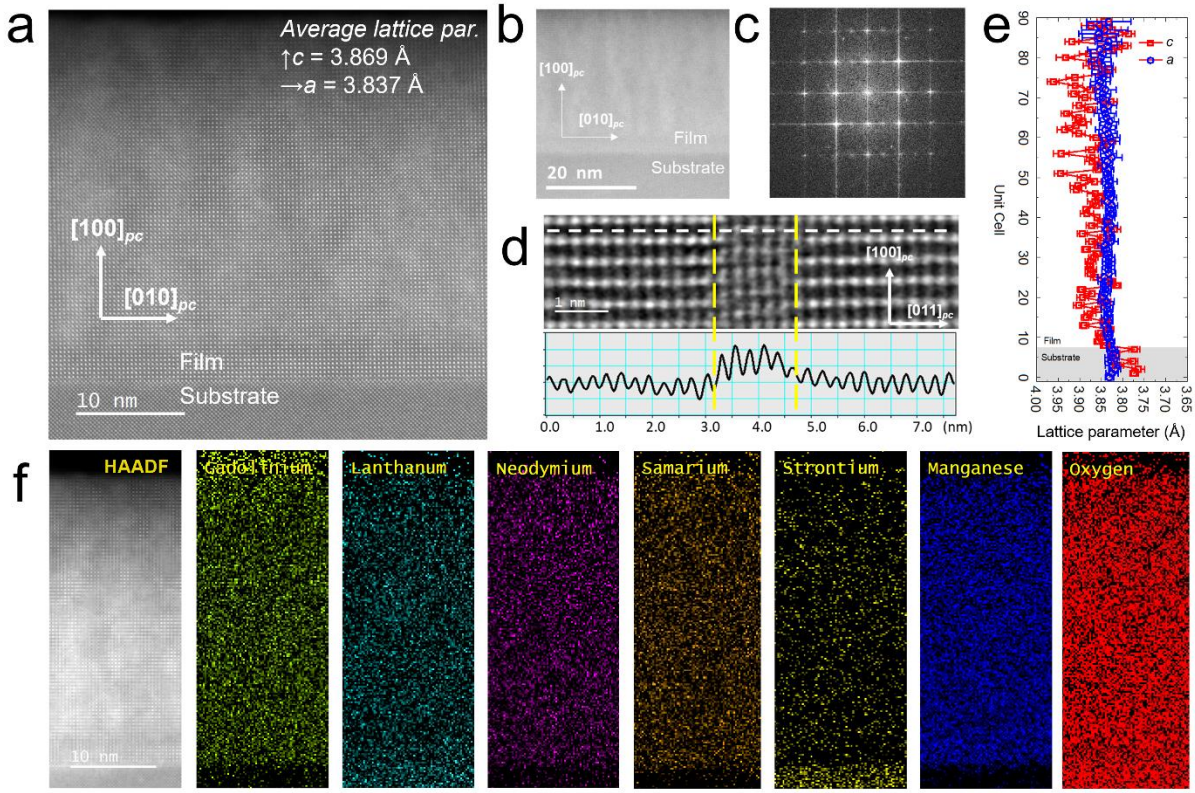

Figure 4. STEM analysis of HE-Mn deposited under $p(O_2)$ = 0.03 mbar. **a**, **b** High resolution HAADF-STEM micrographs along [001] direction, indicating coherent and defect free growth of HE-Mn on LSAT. **c** FFT shows well-defined diffraction spots confirming high crystallinity and epitaxy on LSAT. The elongation of the diffraction spots, along with stronger diffuse scattering and pronounced streaking, supports the presence of columnar defects (RP faults). **d** Detailed view of the nano-columnar RP faults observed in HE-Mn films deposited under $p(O_2)$ = 0.03 mbar, HAADF image along [011] direction. At the RP fault, A-site atoms replace the B-site atoms and vice versa. There is an obvious increase in the contrast of atomic columns highlighted by the white dotted lines across the RP fault (enclosed with the yellow dashed lines). **e** Profile of lattice parameter and unit cell from interface. **f** EDS mapping depicting uniform elemental distribution in HE-Mn films.

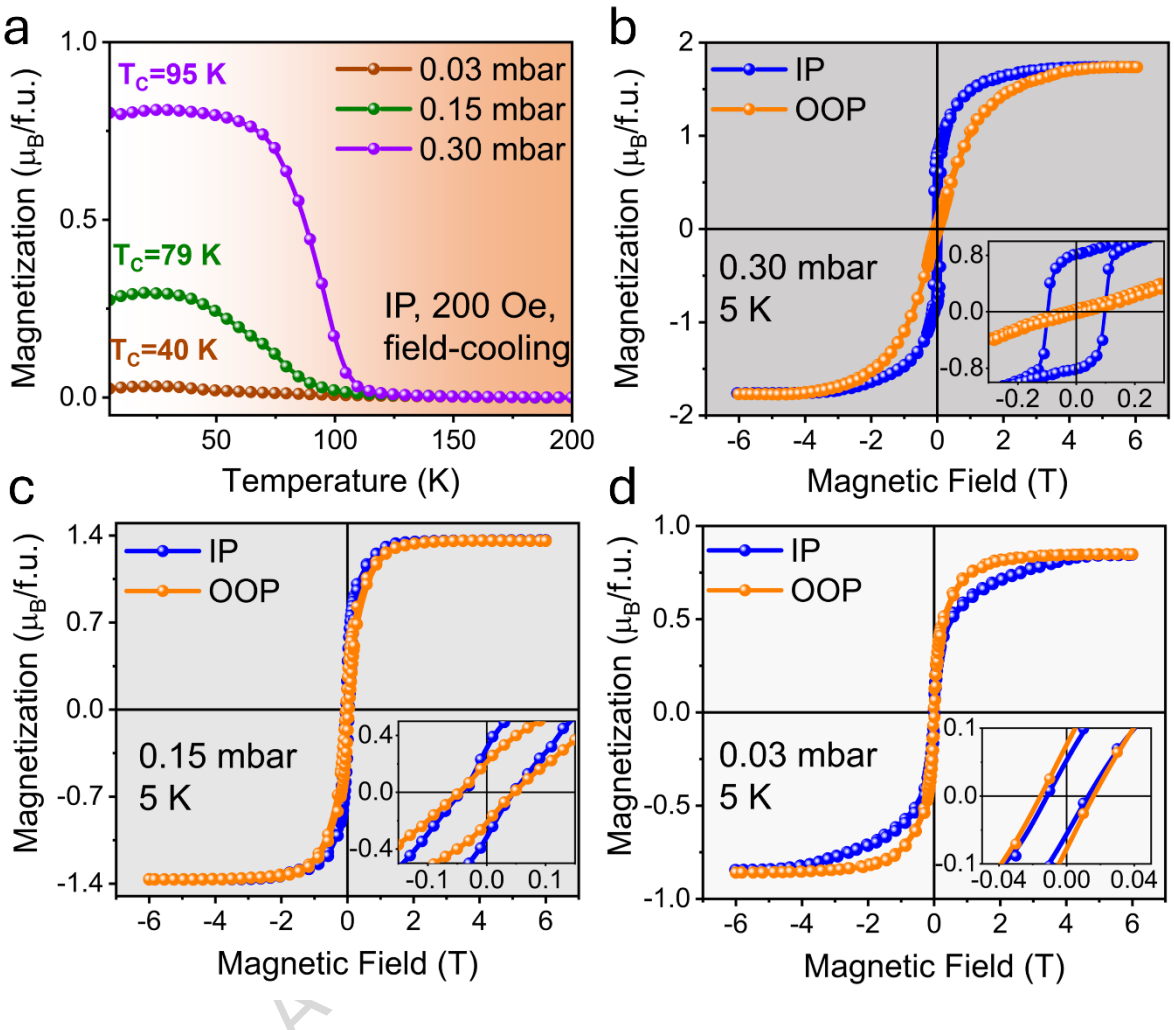

Figure 5. Oxygen vacancies influence on magnetism of HE-Mn /LSAT(001). **a** M-T (FC, 200 Oe, in-plane) of HE-Mn/LSAT(001) with different oxygen deposition partial pressure. **b**, **c**, **d** M-H at 5 K of HE-Mn thin films with $p(O_2)$ of 0.3 mbar, 0.15 mbar and 0.03 mbar, respectively. Inset in **b**, **c**, **d** show the coercive field.

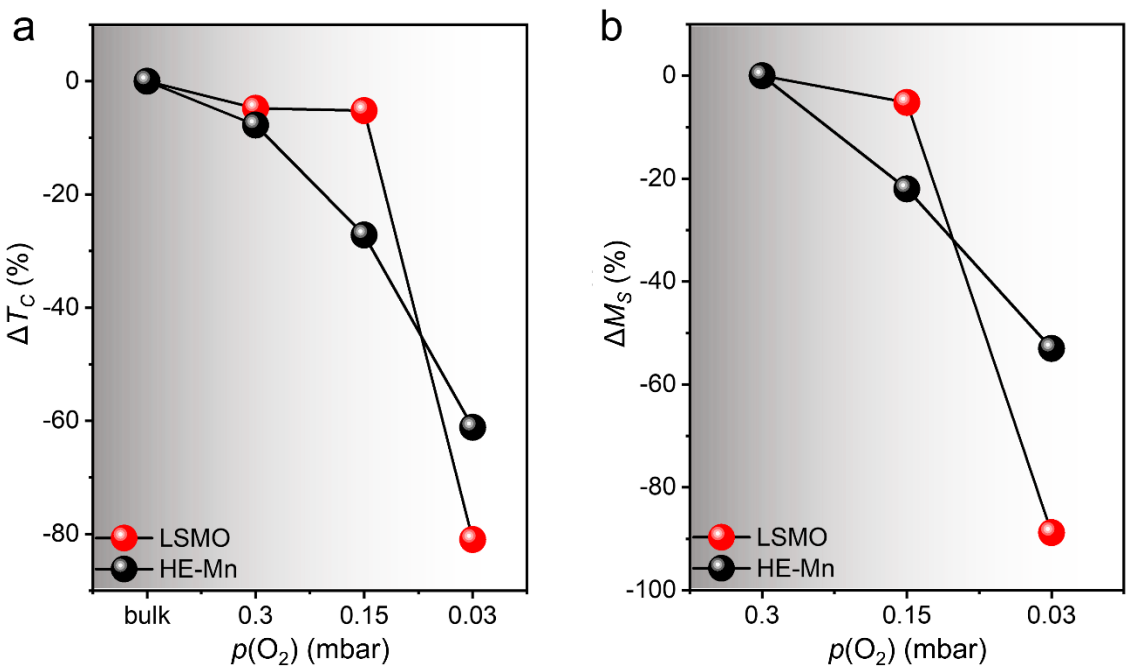

Figure 6. a, **b** Comparison of variation trend of T_C (IP, 200 Oe) and M_S (IP, 5 K), respectively, between LSMO and HE-Mn films as a function of $p(O_2)$, highlighting the much stronger suppression of magnetic ordering in LSMO relative to HE-Mn.

ARTICLE IN PRESS

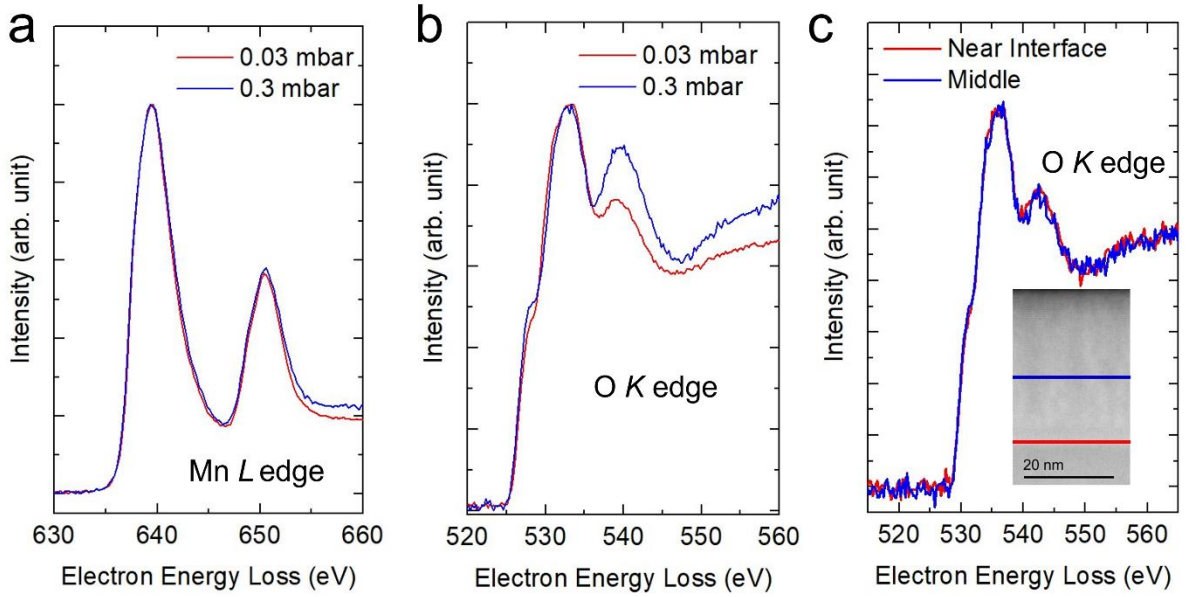

Figure 7. EELS analysis of Mn and O in HE-Mn film deposited at $p(O_2)$ = 0.3 and 0.03 mbar. **a**, **b** indicates the Mn *L*-edge and O *K*-edge spectra, respectively. **c** O K-edge spectra acquired at different positions on the HE-Mn film grown at 0.03 mbar, highlight minimal changes in the M-O bonding across the thickness of the film.

ARTICLE IN PRESS

Editor Summary:

High-entropy oxides offer a novel approach to materials design, yet the role of anion defects in their structure and properties is not well understood. Here, the authors reveal that oxygen non-stoichiometry in high-entropy manganite films induces Ruddlesden-Popper faults and maintains ferromagnetic ordering, highlighting its potential for defect engineering and magnetic tuning.

Peer review information:

Communications Materials thanks the anonymous reviewers for their contribution to the peer review of this work. A peer review file is available.

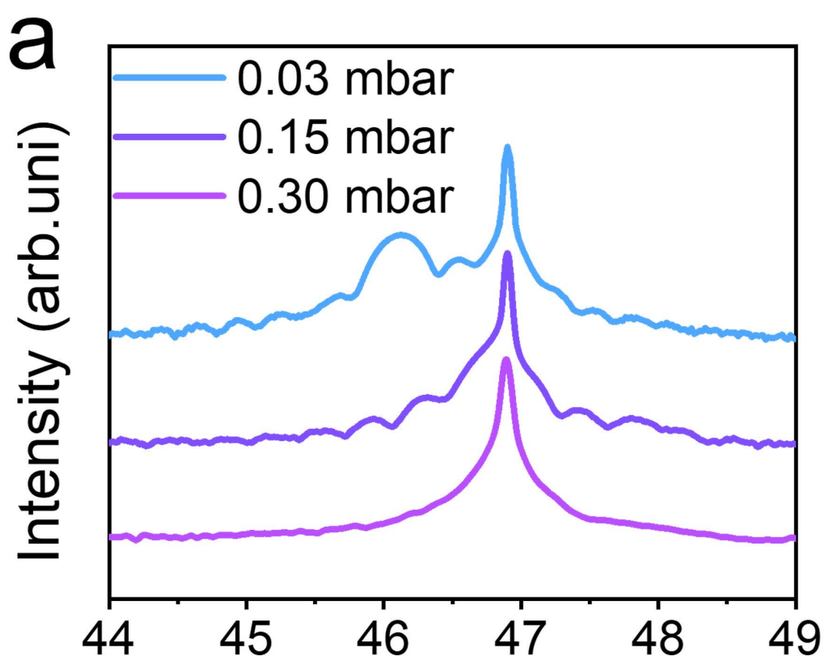
a
0.03 mbar
0.15 mbar
0.30 mbar
Intensity (arb.uni)
44
45
46
47
48
49
2θ (°)

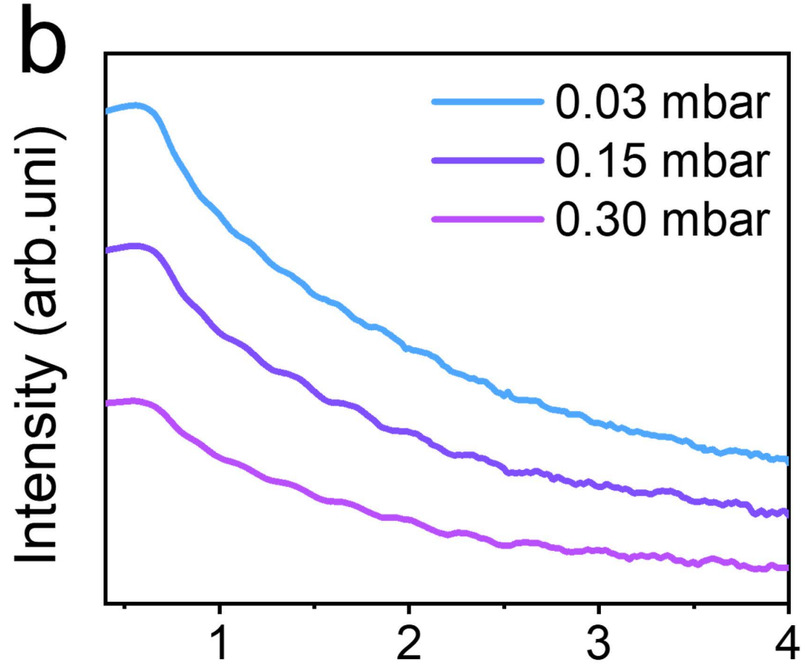
b
0.03 mbar
0.15 mbar
0.30 mbar
Intensity (arb.uni)
1
2
3
4
2θ (°)

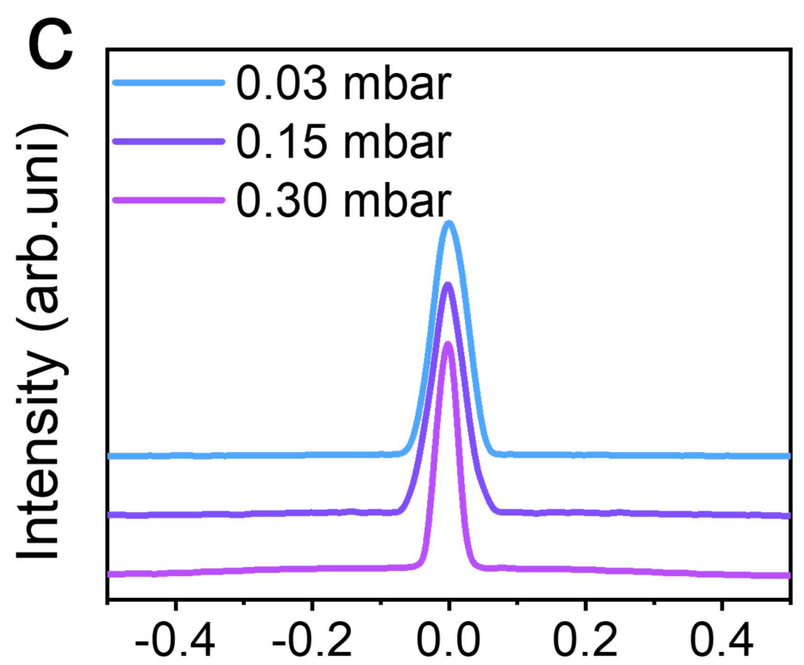
c
0.03 mbar
0.15 mbar
0.30 mbar
Intensity (arb.uni)
-0.4
-0.2
0.0
0.2
0.4
ω–ω0 (°)

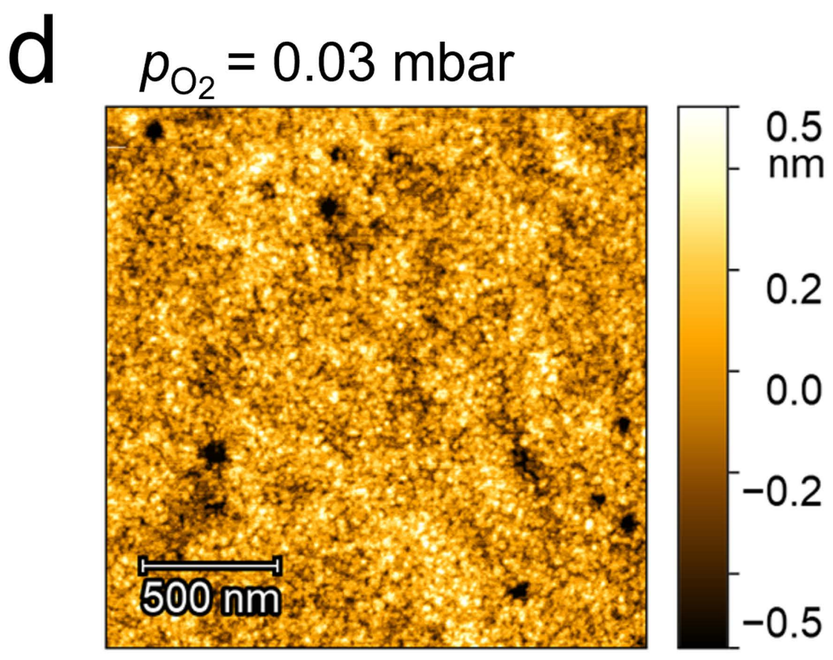
d
pO2 = 0.03 mbar
500 nm
0.5 nm
0.2
0.0
−0.2
−0.5

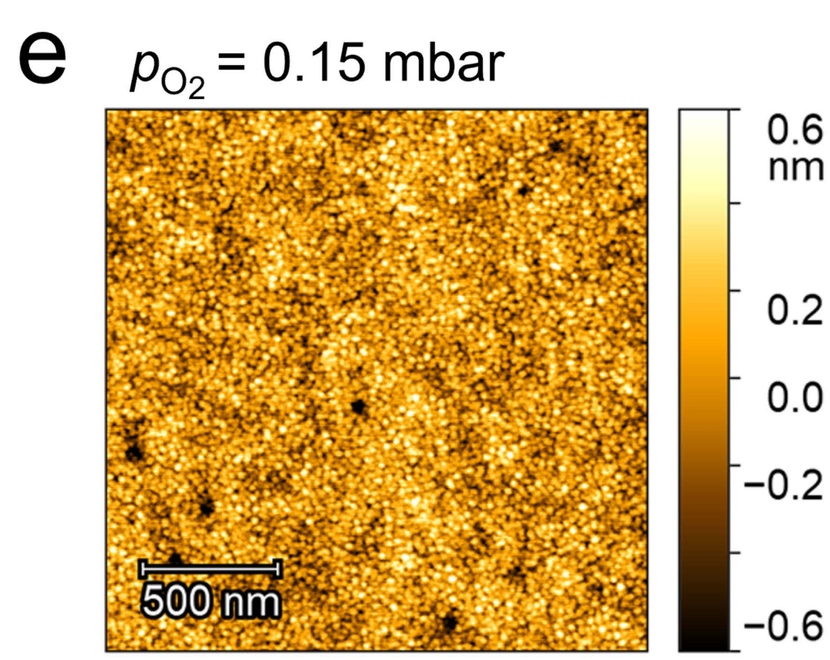
e
pO2 = 0.15 mbar
500 nm
0.6 nm
0.2
0.0
−0.2
−0.6

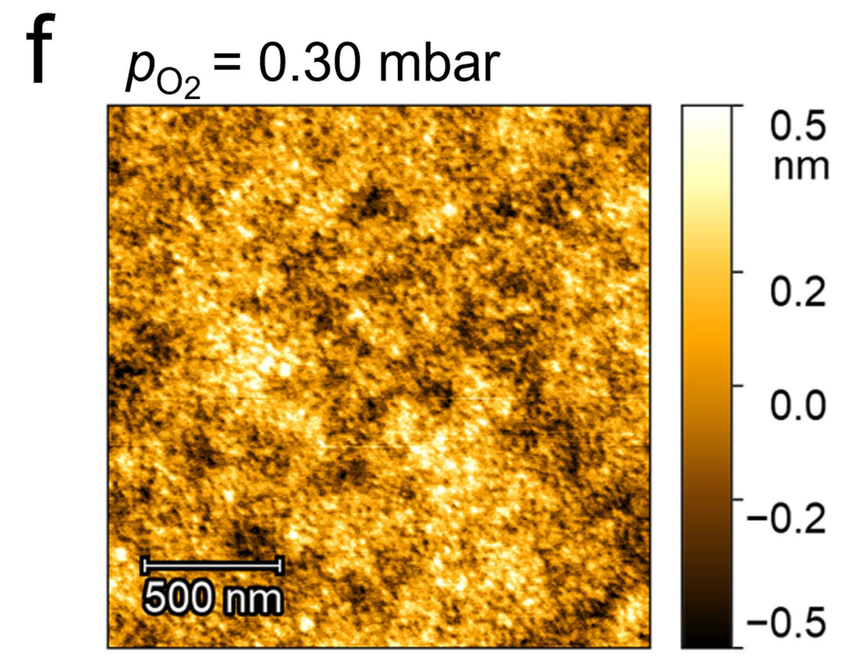
f
pO2 = 0.30 mbar
500 nm
0.5 nm
0.2
0.0
−0.2
−0.5

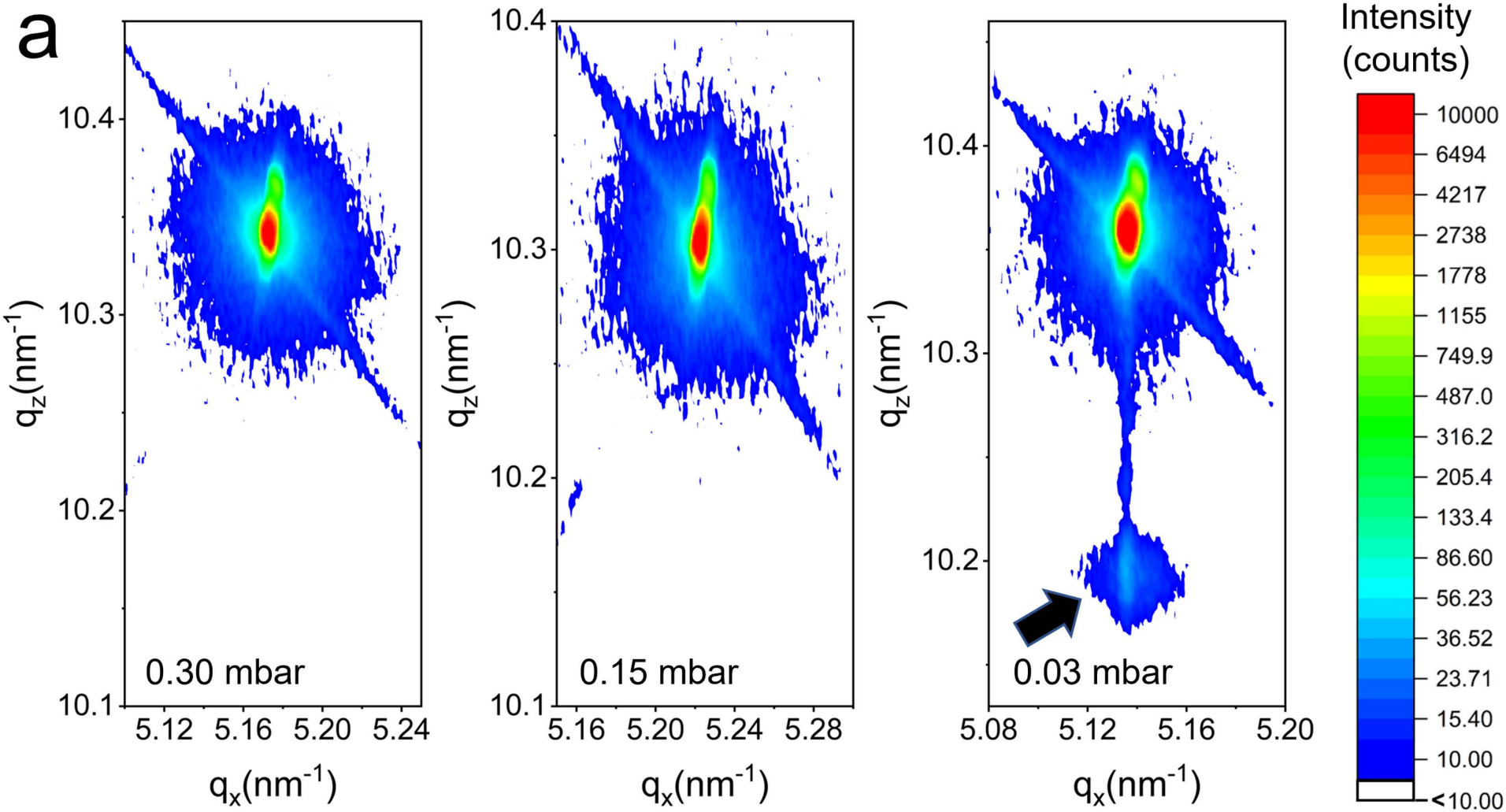
a
0.30 mbar
0.15 mbar
0.03 mbar
q_z(nm^{-1})
q_x(nm^{-1})
Intensity (counts)
10000
6494
4217
2738
1778
1155
749.9
487.0
316.2
205.4
133.4
86.60
56.23
36.52
23.71
15.40
10.00
<10.00
b
a_{zz}: 3.875 Å
3.885 Å
3.893 Å
3.933 Å
bulk
0.30 mbar
0.15 mbar
0.03 mbar
ε_{zz}: 0
0.28 %
0.46%
1.50%

a

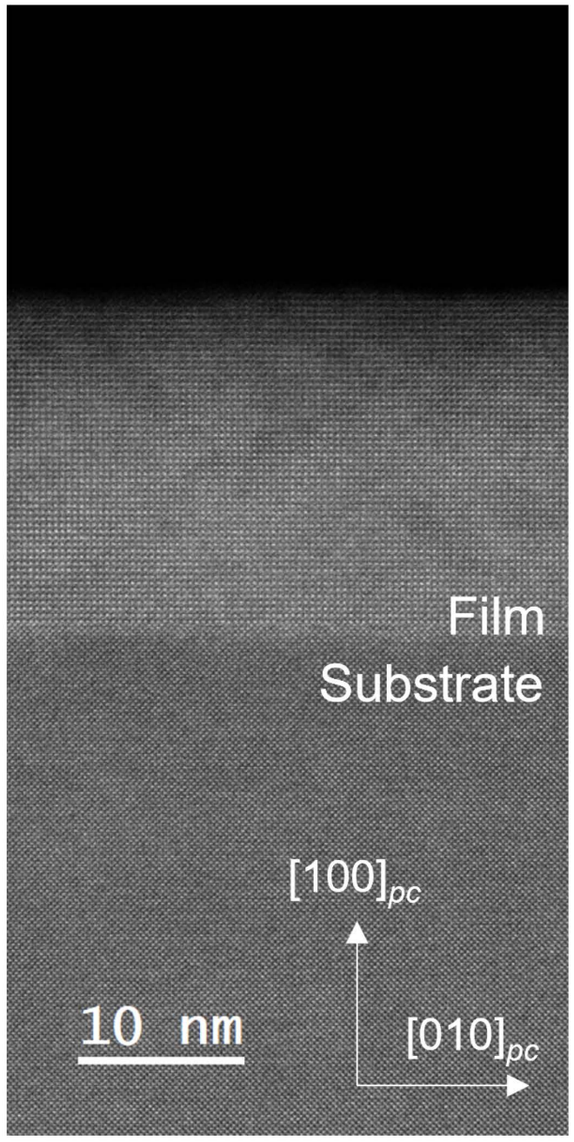
Film
Substrate
[100]pc
[010]pc
10 nm

b

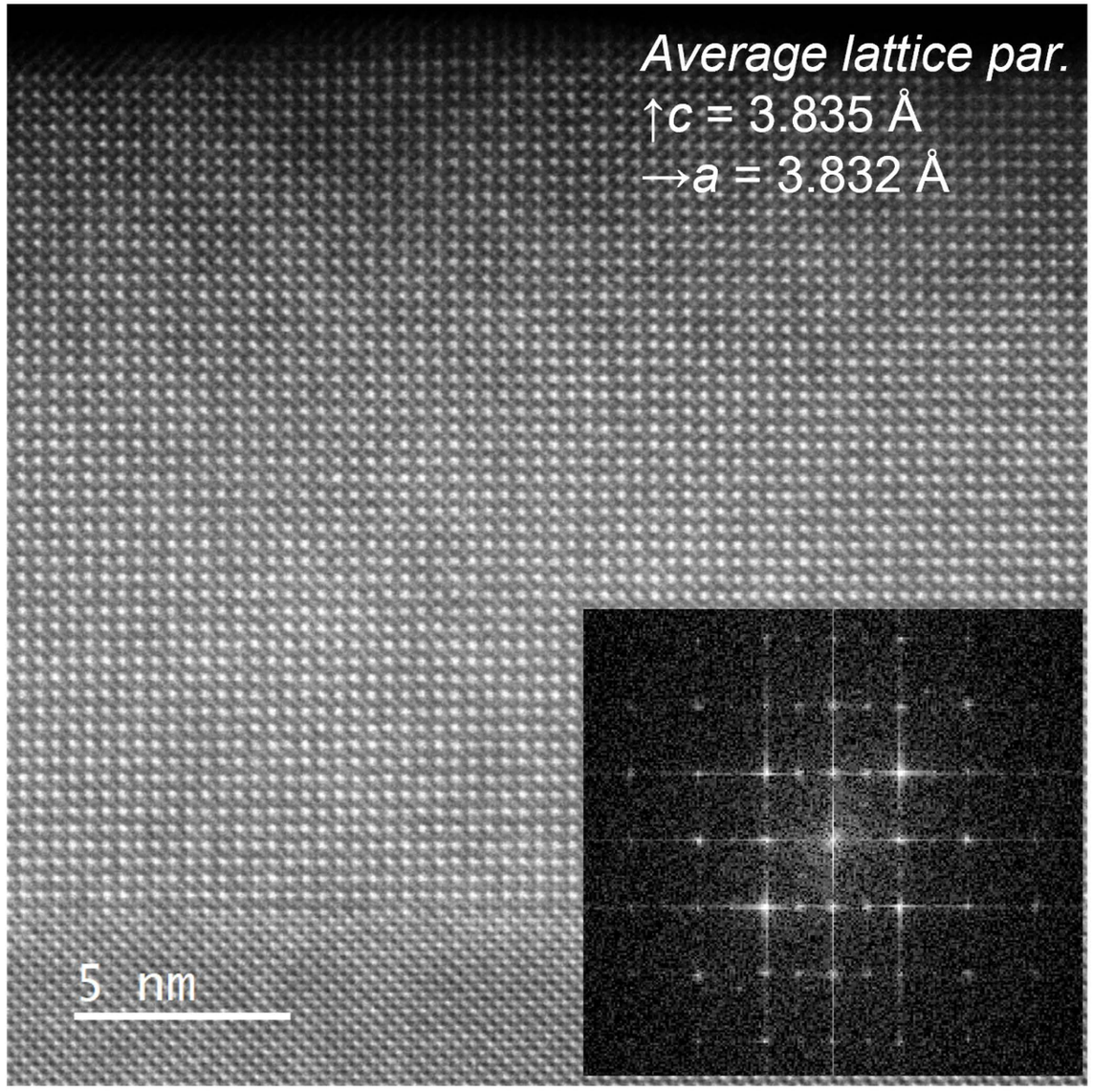
Average lattice par.
↑c = 3.835 Å
→a = 3.832 Å
5 nm

c

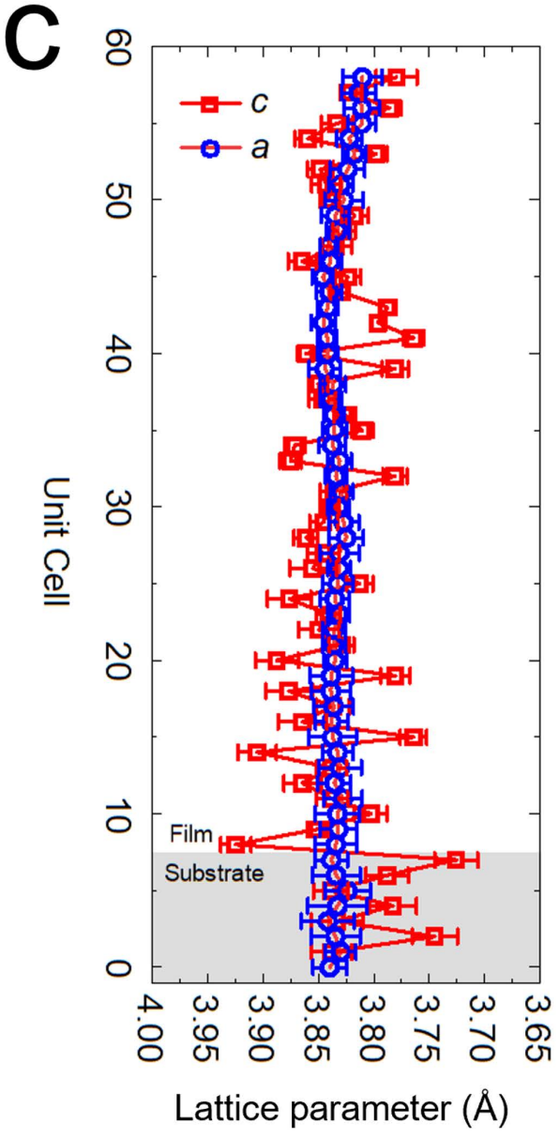
c
a
Film
Substrate
Unit Cell
0
10
20
30
40
50
60
4.00
3.95
3.90
3.85
3.80
3.75
3.70
3.65
Lattice parameter (Å)

d

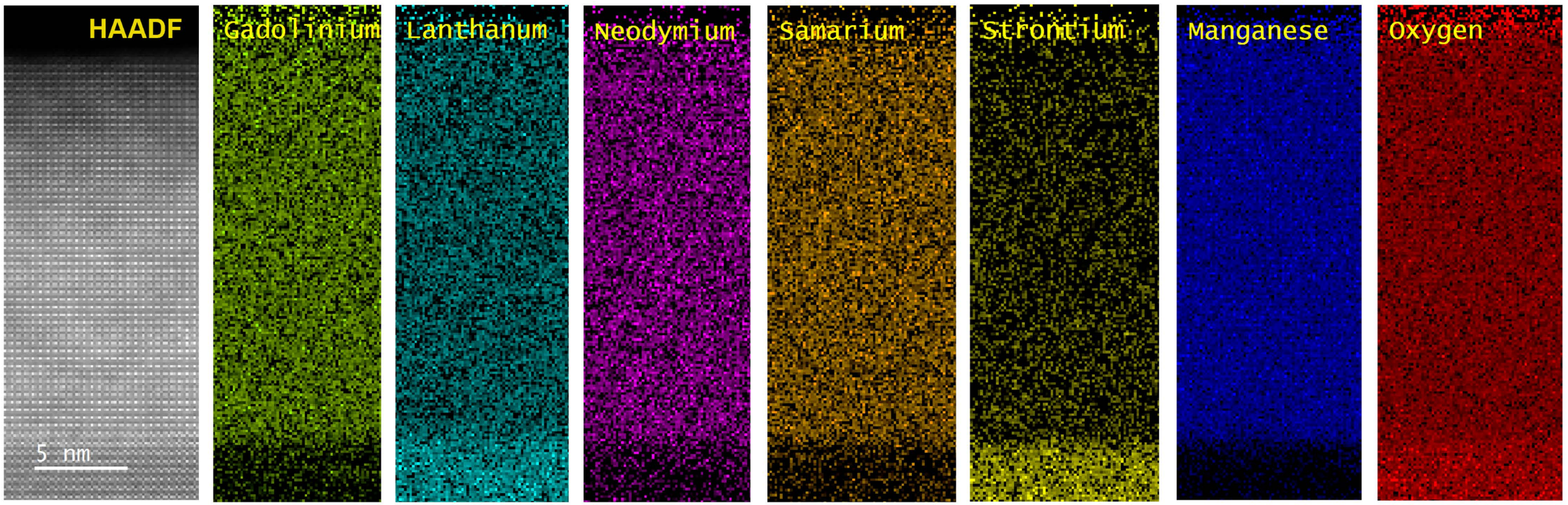
HAADF
5 nm
Gadolinium
Lanthanum
Neodymium
Samarium
Strontium
Manganese
Oxygen

a

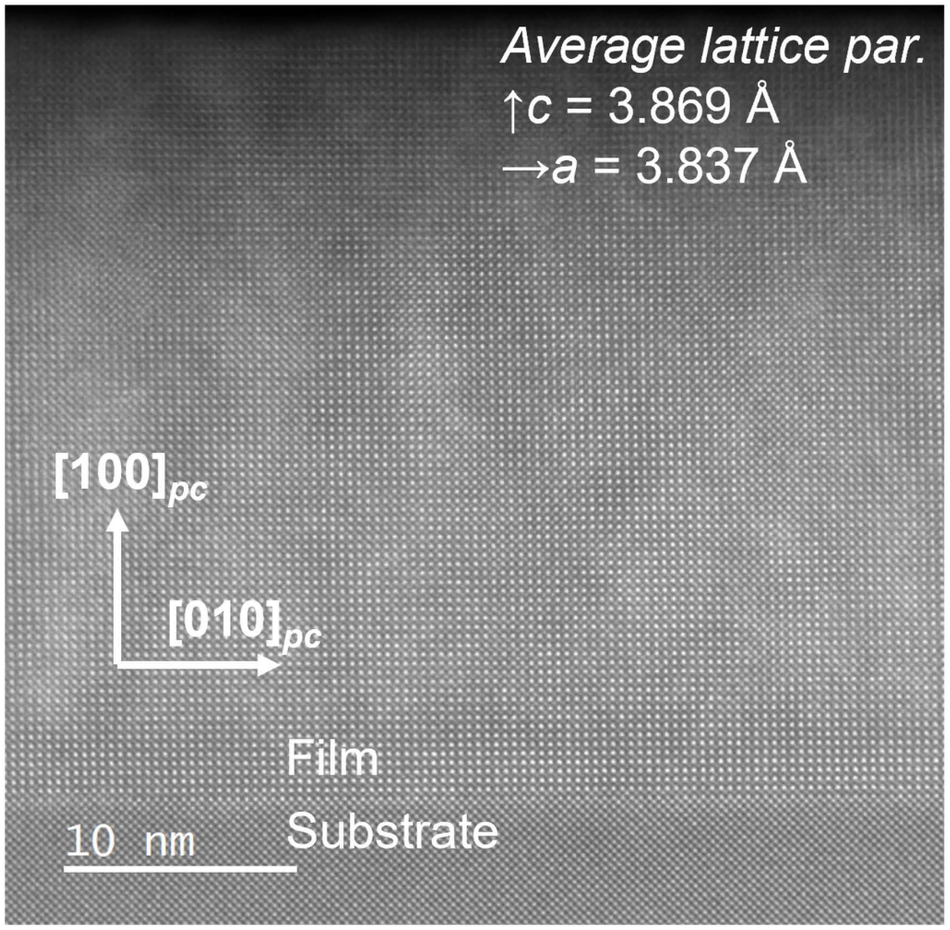
Average lattice par.
↑c = 3.869 Å
→a = 3.837 Å
[100]pc
[010]pc
Film
Substrate
10 nm

b

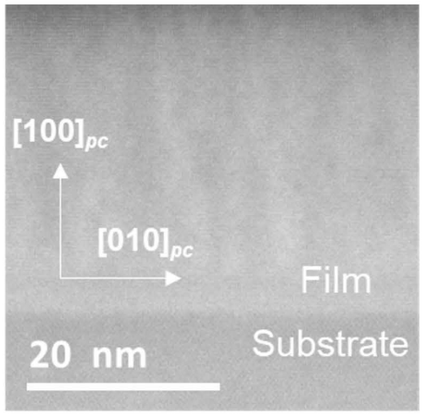
[100]pc
[010]pc
Film
Substrate
20 nm

c

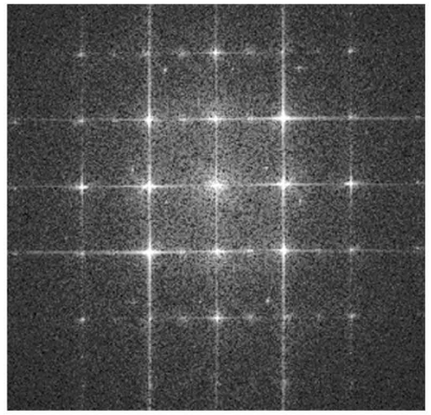

d

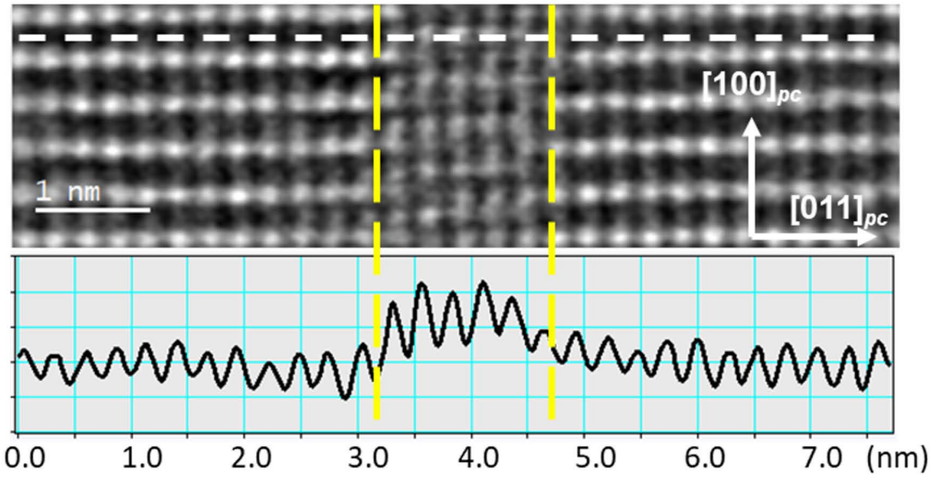
[100]pc
[011]pc
1 nm
0.0
1.0
2.0
3.0
4.0
5.0
6.0
7.0
(nm)

e

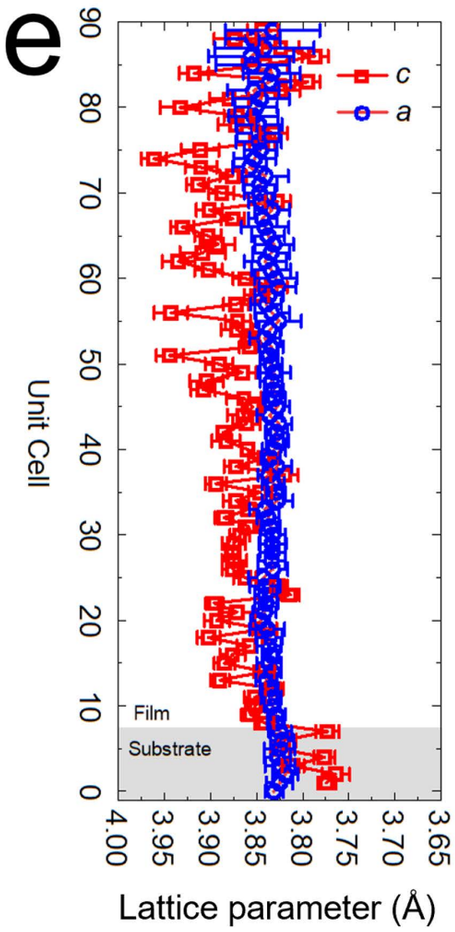
c
a
Unit Cell
Film
Substrate
90
80
70
60
50
40
30
20
10
0
4.00
3.95
3.90
3.85
3.80
3.75
3.70
3.65
Lattice parameter (Å)

f

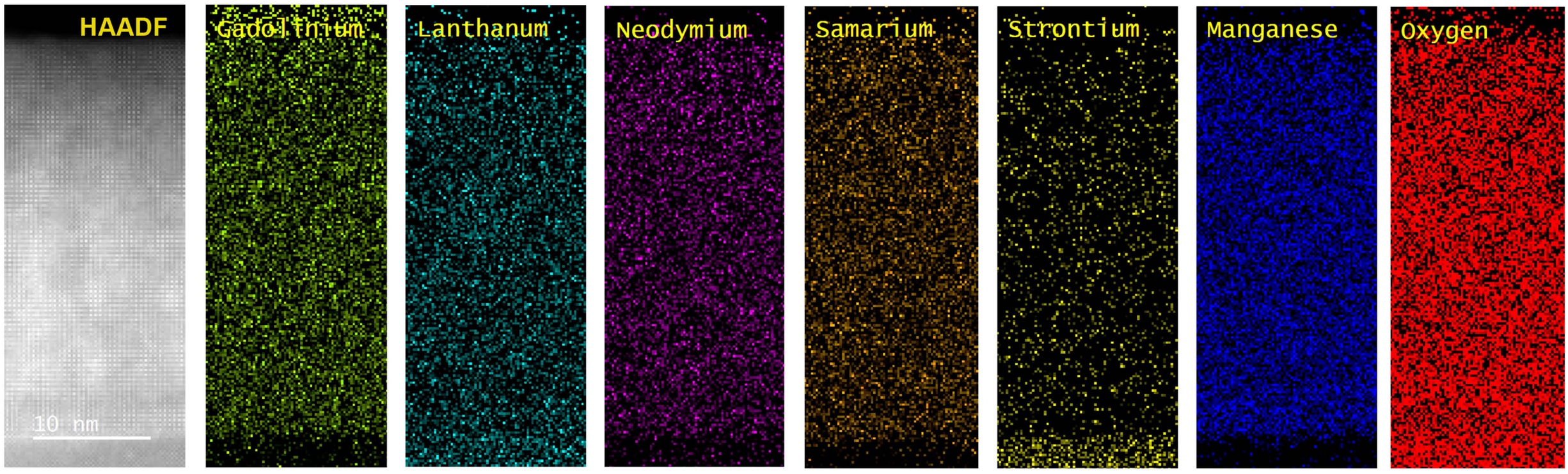
HAADF
10 nm
Gadolinium
Lanthanum
Neodymium
Samarium
Strontium
Manganese
Oxygen

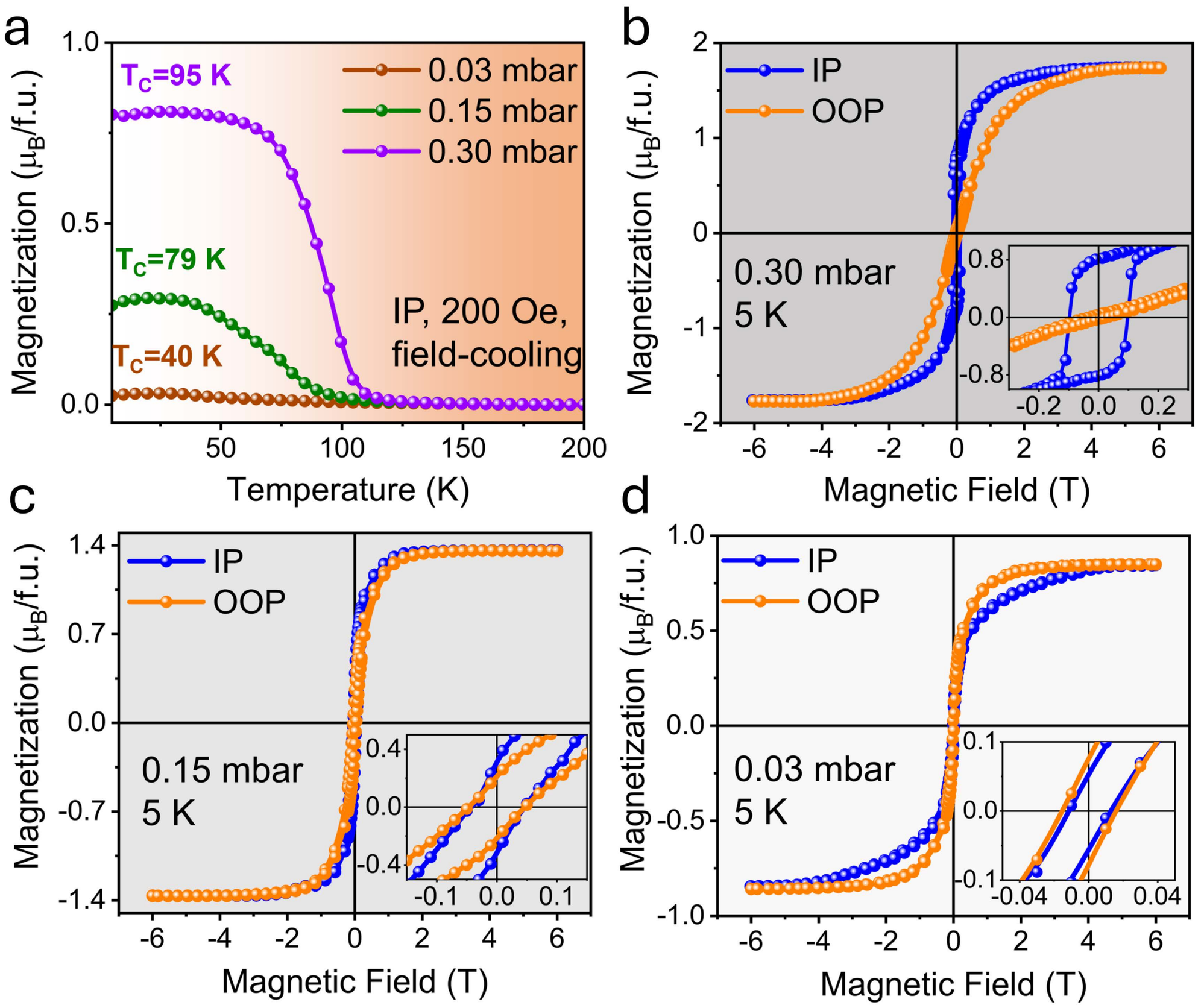
a
Magnetization (μ_B/f.u.)
Temperature (K)
T_C=95 K
T_C=79 K
T_C=40 K
0.03 mbar
0.15 mbar
0.30 mbar
IP, 200 Oe,
field-cooling
b
Magnetization (μ_B/f.u.)
Magnetic Field (T)
IP
OOP
0.30 mbar
5 K
c
Magnetization (μ_B/f.u.)
Magnetic Field (T)
IP
OOP
0.15 mbar
5 K
d
Magnetization (μ_B/f.u.)
Magnetic Field (T)
IP
OOP
0.03 mbar
5 K

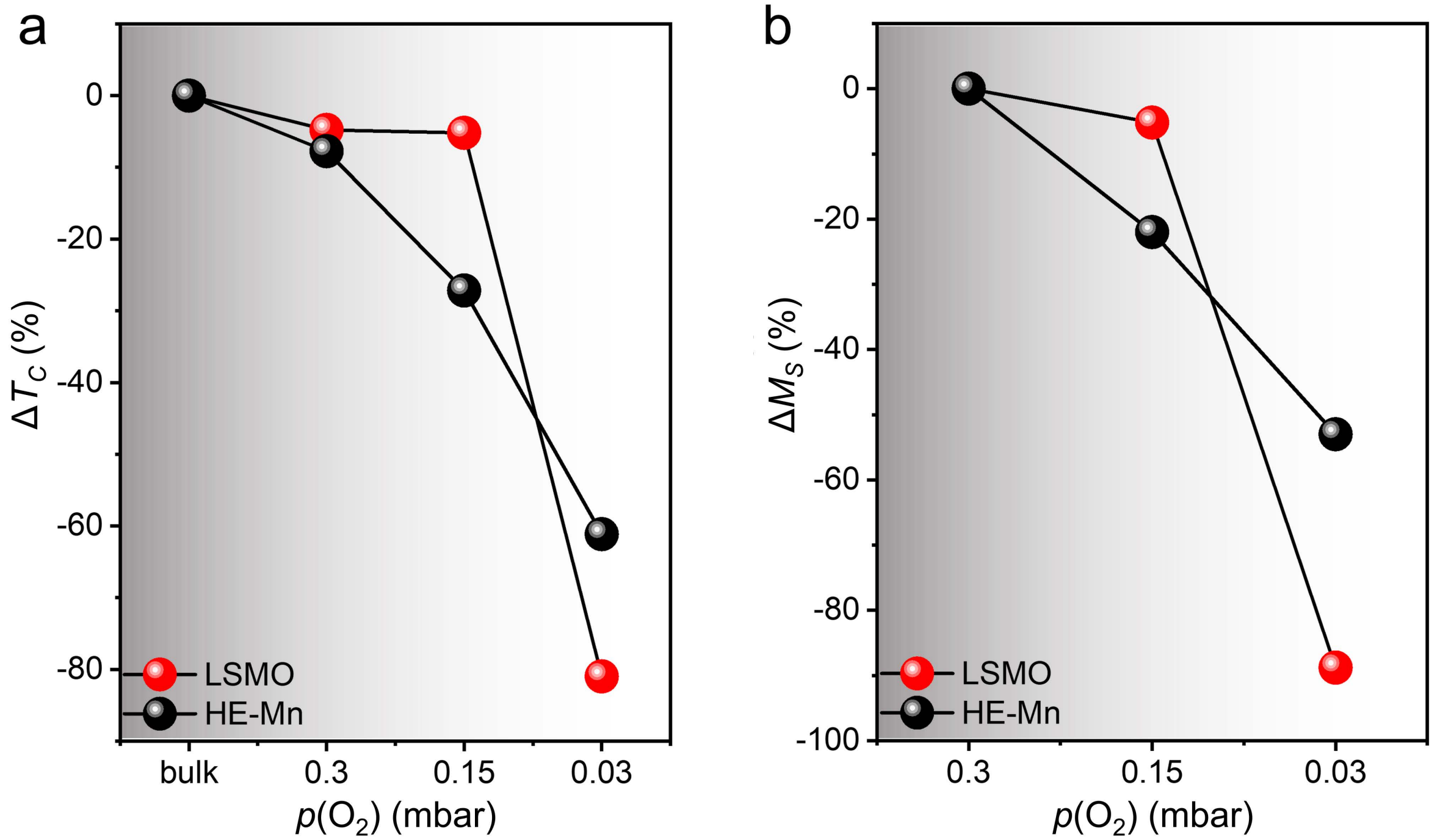
a
0
-20
-40
-60
-80
ΔT_C (%)
LSMO
HE-Mn
bulk
0.3
0.15
0.03
$p(O_2)$ (mbar)
b
0
-20
-40
-60
-80
-100
ΔM_S (%)
LSMO
HE-Mn
0.3
0.15
0.03
$p(O_2)$ (mbar)

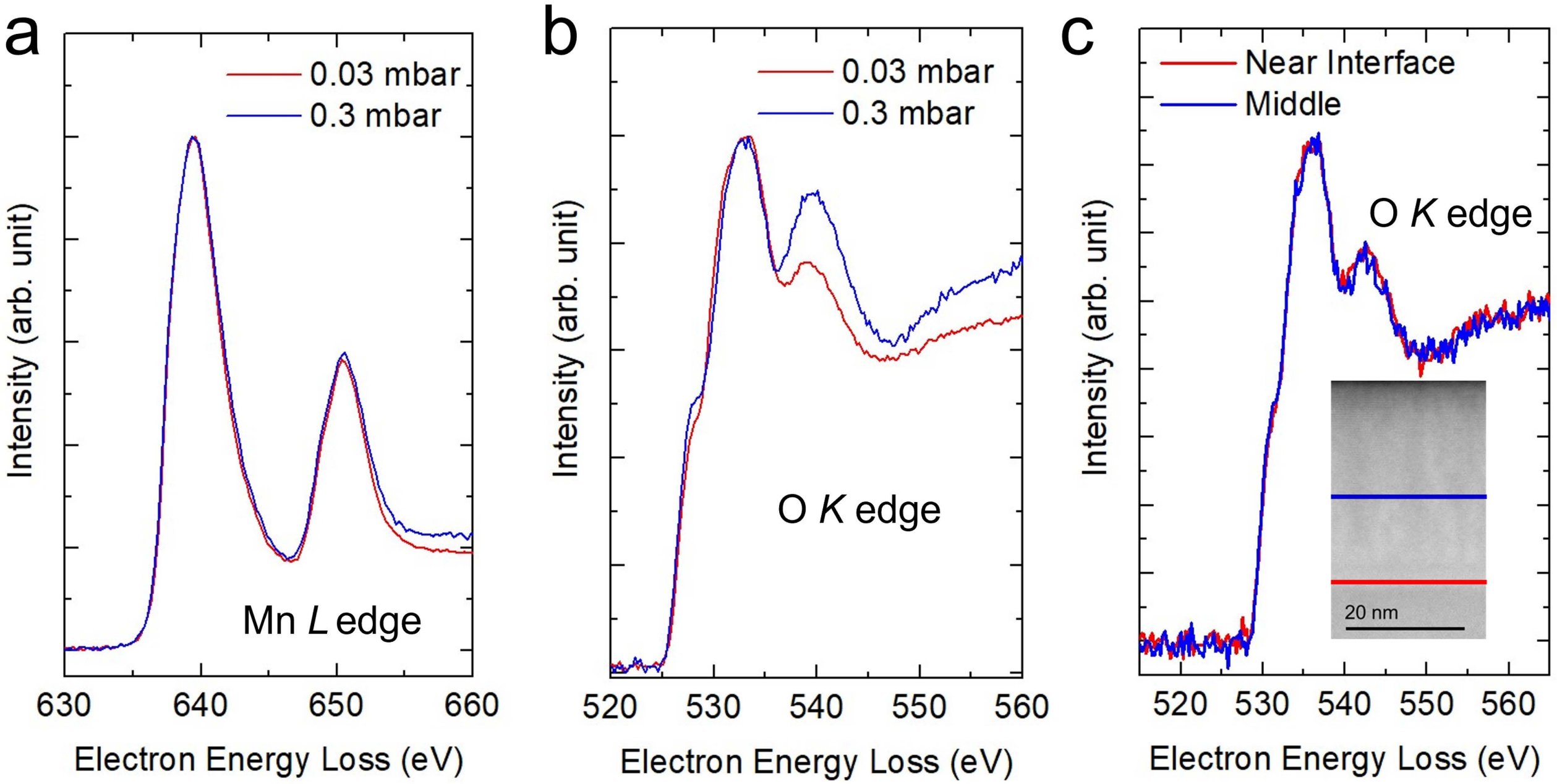
a
0.03 mbar
0.3 mbar
Mn L edge
Intensity (arb. unit)
630
640
650
660
Electron Energy Loss (eV)
b
0.03 mbar
0.3 mbar
O K edge
Intensity (arb. unit)
520
530
540
550
560
Electron Energy Loss (eV)
c
Near Interface
Middle
O K edge
20 nm
Intensity (arb. unit)
520
530
540
550
560
Electron Energy Loss (eV)